

Hayabusa-2 Mission Target Asteroid 162173 Ryugu (1999 JU₃): Searching for the Object's Spin-Axis Orientation[★]

T. G. Müller¹, J. Ďurech², M. Ishiguro³, M. Mueller⁴, T. Krübler¹, H. Yang³, M.-J. Kim⁵, L. O'Rourke⁶, F. Usui⁷, C. Kiss⁸, B. Altieri⁶, B. Carry⁹, Y.-J. Choi⁵, M. Delbo¹⁰, J. P. Emery¹¹, J. Greiner¹, S. Hasegawa¹², J. L. Hora¹³, F. Knust¹, D. Kuroda¹⁴, D. Osip¹⁵, A. Rau¹, A. Rivkin¹⁶, P. Schady¹, J. Thomas-Osip¹⁵, D. Trilling¹⁷, S. Urakawa¹⁸, E. Vilenius¹⁹, P. Weissman²⁰, P. Zeidler²¹

- ¹ Max-Planck-Institut für extraterrestrische Physik, Giessenbachstraße, Postfach 1312, 85741 Garching, Germany; tmueller@mpe.mpg.de
- ² Astronomical Institute, Faculty of Mathematics and Physics, Charles University, V Holešovičkách 2, 180 00, Praha 8, Czech Republic;
- ³ Department of Physics and Astronomy, Seoul National University, Gwanak, Seoul 151-742, Korea
- ⁴ Kapteyn Astronomical Institute, Rijksuniversiteit Groningen, Postbus 800, 9700 AV Groningen, The Netherlands
- ⁵ Korea Astronomy and Space Science Institute, 776 Daedeokdae-ro, Yuseong-gu, 305-348 Daejeon, Korea
- ⁶ European Space Astronomy Centre (ESAC), European Space Agency, 28691 Villanueva de la Cañada, Madrid, Spain
- ⁷ Center for Planetary Science, Graduate School of Science, Kobe University, 7-1-48, Minatogijima-Minamimachi, Chuo-Ku, Kobe 650-0047, Japan
- ⁸ Konkoly Observatory, Research Center for Astronomy and Earth Sciences, Hungarian Academy of Sciences; Konkoly Thege 15-17, H-1121 Budapest, Hungary
- ⁹ IMCCE, Observatoire de Paris, UPMC Paris-06, Université Lille1, UMR8028 CNRS, 77 Av. Denfert Rochereau, 75014 Paris, France
- ¹⁰ Laboratoire Lagrange, UNS-CNRS, Observatoire de la Côte d'Azur, Boulevard de l'Observatoire-CS 34229, 06304 Nice Cedex 4, France
- ¹¹ Earth and Planetary Science Department & Planetary Geosciences Institute, University of Tennessee, Knoxville, TN 37996, USA
- ¹² Institute of Space and Astronautical Science, Japan Aerospace Exploration Agency, 3-1-1 Yoshinodai, Sagami-hara, Kanagawa 229-8510, Japan
- ¹³ Harvard-Smithsonian Center for Astrophysics, 60 Garden Street, MS 65, Cambridge, MA 02138-1516, USA
- ¹⁴ Okayama Astrophysical Observatory, National Astronomical Observatory of Japan, Honjo 3037-5, Kamogata, Asakuchi, Okayama 719-0232, Japan
- ¹⁵ Carnegie Observatories, Las Campanas Observatory, Casilla 60, La Serena, Chile
- ¹⁶ Johns Hopkins University Applied Physics Laboratory, 11101 Johns Hopkins Rd., Laurel, MD 20723, USA
- ¹⁷ Northern Arizona University, Department of Physics and Astronomy, Bldg. 19, Rm. 209, Flagstaff, AZ 86011, United States
- ¹⁸ Bisei Spaceguard Center, Japan Spaceguard Association, 1716-3 Okura, Bisei-cho, Ibara, Okayama 714-1411, Japan
- ¹⁹ Max-Planck-Institut für Sonnensystemforschung, Justus-von-Liebig-Weg 3, 37077 GöttingenMPS, Germany
- ²⁰ Planetary Science Institute, 1700 East Fort Lowell, Suite 106, Tucson, AZ 85719, USA
- ²¹ Astronomisches Rechen-Institut, Zentrum für Astronomie der Universität Heidelberg, Mönchhofstr. 12-14, 69120 Heidelberg, Germany

Received ; accepted

ABSTRACT

The JAXA Hayabusa-2 mission was approved in 2010 and launched on December 3, 2014. The spacecraft will arrive at the near-Earth asteroid 162173 Ryugu (1999 JU₃) in 2018 where it will perform a survey, land and obtain surface material, then depart in December 2019 and return to Earth in December 2020. We observed Ryugu with the Herschel Space Observatory in April 2012 at far-infrared thermal wavelengths, supported by several ground-based observations to obtain optical lightcurves. We reanalysed previously published Subaru-COMICS and AKARI-IRC observations and merged them with a Spitzer-IRS data set. In addition, we used a large set of Spitzer-IRAC observations obtained in the period January to May, 2013. The data set includes two complete rotational lightcurves and a series of ten "point-and-shoot" observations, all at 3.6 and 4.5 μm . The almost spherical shape of the target together with the insufficient lightcurve quality forced us to combine radiometric and lightcurve inversion techniques in different ways to find the object's spin-axis orientation, its shape and to improve the quality of the key physical and thermal parameters. Handling thermal data in inversion techniques remains challenging: thermal inertia, roughness or local structures influence the temperature distribution on the surface. The constraints for size, spin or thermal properties therefore heavily depend on the wavelengths of the observations. We find that the solution which best matches our data sets leads to this C class asteroid having a retrograde rotation with a spin-axis orientation of ($\lambda = 310^\circ - 340^\circ$; $\beta = -40^\circ \pm \sim 15^\circ$) in ecliptic coordinates, an effective diameter (of an equal-volume sphere) of 850 to 880 m, a geometric albedo of 0.044 to 0.050 and a thermal inertia in the range 150 to 300 J m⁻² s^{-0.5} K⁻¹. Based on estimated thermal conductivities of the top-layer surface in the range 0.1 to 0.6 W K⁻¹ m⁻¹, we calculated that the grain sizes are approximately equal to between 1 and 10 mm. The finely constrained values for this asteroid serve as a 'design reference model', which is currently used for various planning, operational and modelling purposes by the Hayabusa2 team.

Key words. Minor planets, asteroids: individual – Radiation mechanisms: Thermal – Techniques: photometric – Infrared: planetary systems

1. Introduction

Remote observations and in-situ measurements of asteroids are considered highly complementary in nature: remote sensing shows the global picture, but transforming measured fluxes in physical quantities frequently depends upon model assumptions to describe surface properties. In-situ techniques measure physical quantities, such as size, shape, rotational properties, geometric albedo or surface details, in a more direct way. However, in-situ techniques are often limited in spatial/rotational/aspect coverage (flybys) and wavelength coverage (mainly visual and near-IR wavelengths). Mission targets are therefore important objects for a comparison of properties derived from disk-integrated measurements taken before arrival at the asteroid with those produced as output of the in-situ measurements. The associated benefits are obvious: (i) the model techniques and output accuracies for remote, disk-integrated observations can be validated (e.g., Müller et al. 2014 for the Hayabusa mission target 25143 Itokawa or O'Rourke et al. 2012 for the Rosetta flyby target 21 Lutetia); (ii) the model techniques can then be applied to many similar objects which are not included in interplanetary mission studies, but easily accessible by remote observations. The pre-mission observations are also important for determining the object's thermal and physical conditions in support for the construction of the spacecraft and its instruments, and to prepare flyby, orbiting and landing scenarios.

The JAXA Hayabusa-2 mission, approved in 2010, was successfully launched on Dec. 3, 2014. It is expected to arrive at the asteroid 162173 Ryugu in 2018, survey the asteroid for a year and a half, then land and obtain surface material, and finally depart in December 2019, returning to Earth in December 2020.

For various Hayabusa-2 planning, operational and modelling activities, it is crucial to know at least the basic characteristics of the mission target asteroid. Previous publications (Table 1) presented shape solutions close to a sphere and a rotation period of approximately 7.63 h, but a range of possible solutions for Ryugu's spin properties which were then tested against visual lightcurves and various sets of thermal data, using different thermal models and assumptions for Ryugu's surface properties:

- Hasegawa et al. (2008) assumed an equator-on observing geometry (prograde rotation) for their radiometric analysis and fitted a small set of thermal measurements (AKARI, Subaru).
- Abe et al. (2008) found $(\lambda, \beta)_{ecl} = (331.0^\circ, +20^\circ)$ and $(327.3^\circ, +34.7^\circ)$, indicating a prograde rotation. The solutions were based on applying two different methods (epoch and amplitude methods) to the available set of visual lightcurves.
- Campins et al. (2009) were using the Abe et al. (2008) spin-axis solution, but also tested an extreme case of an equatorial retrograde geometry $(\lambda, \beta)_{ecl} = (80^\circ, -80^\circ)$ against a single-epoch Spitzer-IRS spectrum.
- Müller et al. (2011a) derived three possible solutions for the spin-axis orientation based on a subset of the currently existing data, but assuming a very high (and probably un-

realistic) surface roughness: $(\lambda, \beta)_{ecl} = (73^\circ, -62^\circ)$, $(69.6^\circ, -56.7^\circ)$, and $(77.1^\circ, -30.9^\circ)$.

- Yu et al. (2014) reconstructed a shape model (from low-quality MPC photometric points) under the assumption of a rotation axis orientation with $(73^\circ, -62^\circ)_{ecl}$ and re-interpreted previously published thermal measurements.

The radiometric studies have been performed using ground and space-based observations (Table 1 and references therein). Disk-integrated thermal observations from ground (Subaru) and space (AKARI, Spitzer) were combined with studies on reflected light (light curves, phase curves and colours). Most studies agree on the object's effective diameter of ≈ 900 m, a geometric V-band albedo of 6-8%, an almost spherical shape (related to its low lightcurve amplitude) with a sidereal rotation period of approximately 7.63 h and a thermal inertia in the range $150 - 1000 \text{ J m}^{-2} \text{ s}^{-0.5} \text{ K}^{-1}$. A low-resolution near-IR spectrum (Pinilla-Alonso et al. 2013) confirmed the primitive nature of the C-type object Ryugu. Two independent studies on the rotational characterisation of the Hayabusa2 target asteroid (Lazzaro et al. 2013; Moskovitz et al. 2013) found featureless spectra with very little variation, indicating a nearly homogeneous surface. However, one key element necessary for detailed mission planning and a final radiometric analysis was still not settled: the object's spin-axis orientation.

The shape and spin properties of an asteroid are typically derived from inversion techniques (Kaasalainen & Torppa 2001; Kaasalainen et al. 2001) on the basis of multi-aspect light curve observations. This procedure was previously applied to 162173 Ryugu and the results were presented by Müller et al. (2011a). We repeated the analysis this time using the large, recently obtained set of visual lightcurves. The full data set of lightcurves includes measurements taken between July 2007 and July 2012, covering a wide range of phase and aspect angles. But the very shallow light curve amplitudes and the insufficient quality of many observations did not allow us to derive a unique solution for the object's spin-axis orientation. Wide ranges of pro- and retrograde orientations combined with different shape models are compatible (in the least-square sense) with the combined data set of all available lightcurves.

This forced us to combine lightcurve inversion techniques with radiometric methods in a new way to find the object's spin-axis orientation, its shape and to improve the quality of the key physical and thermal parameters of 162173 Ryugu.

In Section 2 we present new thermal observations obtained by Herschel-PACS, re-analysed and re-calibrated AKARI-IRC and ground-based Subaru observations and Spitzer-IRAC observations at 3.6 and 4.5 μm . Ground-based, multi-band visual observations are described in Section 3. In Section 4 we describe our new approach to solve for the object's properties. First, we present the search for the object's spin-axis orientation using only the thermal measurements in combination with a spherical shape model (Section 4.1). In a more sophisticated second step (Section 4.2) we use all thermal and visual-wavelength photometric data together and allow for more complex object shapes in our search for the spin axis. In Section 5 we use the best shape and spin-axis information to derive additional physical and thermal properties, and then discuss the results. We conclude in Section 6 by presenting the derived object properties and discuss our experience in combining lightcurve inversion and radiometric techniques, which is applicable to other targets and will help in defining better observing strategies.

* This work includes space data from (i) *Herschel*, an ESA space observatory with science instruments provided by European-led Principal Investigator consortia and with important participation from NASA; (ii) Spitzer Space Telescope, which is operated by the Jet Propulsion Laboratory, California Institute of Technology under a contract with NASA; (iii) AKARI, a JAXA project with the participation of ESA.

Table 1. Summary of previously published thermal and physical properties of 162173 Ryugu

D_{eff} [km]	p_v	shape	spin properties (fixed)	Γ [$\text{Jm}^{-2}\text{s}^{-0.5}\text{K}^{-1}$]	Reference
0.92 ± 0.12	$0.063^{+0.020}_{-0.015}$	a/b=1.21, b/c=1.0	prograde, obliquity 0° , $P_{sid}=7.62722$ h	>500	Hasegawa et al. (2008)
0.90 ± 0.14	0.07 ± 0.01	spherical shape	(1) equatorial view, retrograde	>150	Campins et al. (2009)
"	"	"	(2) $\lambda_{ecl}=331^\circ$, $\beta_{ecl}=+20^\circ$; $P_{sid}=7.62720$ h	700 ± 200	"
0.87 ± 0.03	0.070 ± 0.006	spherical shape	$\lambda_{ecl}=73^\circ$, $\beta_{ecl}=-62^\circ$, $P_{sid}=7.63$ h	200-600	Müller et al. (2011a)
1.13 ± 0.03	0.042 ± 0.003	polyhedron	$\lambda_{ecl}=73^\circ$, $\beta_{ecl}=-62^\circ$, P_{sid} not given	300 ± 50	Yu et al. (2014)

2. Thermal observations of 162173 Ryugu

2.1. Herschel PACS observations

The European Space Agency's (ESA) Herschel Space Observatory (Pilbratt et al. 2010) performed observations from the 2nd Lagrangian point (L2) at 1.5×10^6 km from Earth during the operational phase from 2009 to 2013. It has three science instruments on board covering the far-infrared part of the spectrum not accessible from the ground. The Photodetector Array Camera and Spectrometer (PACS; Poglitsch et al. 2010) was used to observe 162173 Ryugu as part of the "Measurements of 11 Asteroids & Comets" program (MACH-11, O'Rourke et al. 2014). PACS observed the asteroid in early April of 2012 for approximately 1.3 h, split into two separate measurements and taken in solar-system-object tracking mode. The target at this time moved at a Herschel-centric apparent speed of $34''/\text{h}$, corresponding to $19.3''$ movement between the mid-times of both observations. The observations were performed in the $70/160\mu\text{m}$ filter combination to get the best possible S/N in both bands. We selected seven repetitions in each of the two scan-directions for a better characterisation of the background and therefore a more accurate object flux.

The PACS measurements were reduced and calibrated in a standard way as part of the Herschel data pipeline processing. Further processing was then performed as follows. We produced single repetition images from both scan direction measurements: scanA1...scanA7, scanB1...scanB7, not correcting for the apparent motion of the target (it is slow enough that the movement is not visible in a single 282s repetition). We then subtracted from each scanA_n image the respective, single repetition scanB_n image: $\text{diff}_1 = \text{scanA1} - \text{scanB1}, \dots, \text{diff}_7 = \text{scanA7} - \text{scanB7}$, producing differential ("diff") images.

At this point, we co-added the diff images in such a way that each diff image was shifted by the corresponding apparent motion, relative to the first diff image. We produced the double-differential image and then performed the photometry and determined the noise using the implanted source method (Kiss et al. 2014 and references therein) on the final image. It was not feasible to extract the data from the red ($160\mu\text{m}$) image due to the strongly enhanced cirrus background at that wavelength. The final $160\mu\text{m}$ differential image had an estimated confusion noise level of approximately 7 mJy, more than a factor of two higher than the expected source flux.

The final derived flux was aperture and colour corrected to obtain monochromatic flux densities at the PACS reference wavelengths. The colour correction value for 162173 Ryugu of 1.005 in the blue band ($70\mu\text{m}$) is based on a thermophysical model spectral energy distribution (SED), corresponding to an approximately 250 K black-body curve (Poglitsch et al. 2010).

The flux calibration was verified by a set of five high-quality fiducial stars (β And, α Cet, α Tau, α Boo and γ Dra), which have been observed multiple times in the same PACS observing mode as our observations (Balog et al. 2014) and which led to an absolute flux accuracy of 5% for standard PACS photometer observations. Table 2 provides the Herschel observation data set, accompanying information and results.

2.2. Re-analysis of AKARI-IRC observations

The AKARI observations were included in work by Hasegawa et al. (2008) and also used by Müller et al. (2011a) and amount to a single-epoch data set from the IRC instrument with measurements at 15 and $24\mu\text{m}$. These measurements were reanalysed with the 2015 release of the imaging data reduction toolkit¹ (Egusa et al. 2016). The flux calibration is described by Tanabe et al. (2008). The new L15 flux is approximately 7% lower than the previous value in Hasegawa et al. (2008), while the L24 flux is almost identical (Table 3).

2.3. Re-analysis of Subaru-COMICS observations

The Ryugu observations were described in detail by Hasegawa et al. (2008) and also used by Müller et al. (2011a). Here, we re-analysed all data with a more representative handling of the variable atmospheric conditions during the five hours (10:30 - 15:30 UT) of observations on the 28th August, 2007. Using the CFHT skyprobe², we found that the sky was generally stable to an accuracy of $< \sim 0.05$ mag, but sporadically attenuated by > 0.1 mag, probably caused by the passage of thin clouds. Although the skyprobe operates at optical wavelengths, it certainly affected the N-band photometry as well.

For the data reduction we followed the latest version (from Nov. 2012) of the COMICS cookbook³. Here we put special emphasis on the construction of time-varying sky flats, a very critical element for the final accuracy of the derived fluxes. With this new element we could recover the flux of a standard star, placed at different detector positions and observed multiple times during our campaign, on a 3% level. The monitoring of the calibration star 66 Peg (HD 220363) allowed us to establish the instrumental magnitudes at the times of the Ryugu observations. Finally, we conducted aperture photometry for the standard star and our target with different aperture sizes. Colour corrections are typically only on a 1-3% level (Hasegawa et al. 2008; Müller et al. 2004), but depend on the object's spectral energy distribution and the at-

¹ AKARI IRC imaging toolkit version 20150331

² http://www.cfht.hawaii.edu/cgi-bin/elixir/skyprobe.pl?plot&mc1_20070828.png

³ http://www.naoj.org/Observing/DataReduction/-Cookbooks/COMICS_CookBook2p2E.pdf

Table 2. Herschel PACS observations of 162173 Ryugu as part of the GT1_lorourke programme executed on operational day OD 1057 under the observation identifier OBSID 1342243716 & 1342243717. The data were taken with the mini-scan map mode at a scan speed of 20''/s and scan angles, with respect to the instrument, of 70° and 110°, in the blue (70 μm) and red (160 μm) bands simultaneously. Note, that phase angles α are positive before, and negative after opposition. λ_c is the central reference wavelength and FD is the monochromatic and colour-corrected flux density at λ_c .

OD	OBSID	Start time	Duration [s]	Bands	Scan-angle	
1057	1342243716	2012-04-05T00:48:20	1978	70/160	70°	
1057	1342243717	2012-04-05T01:22:21	1978	70/160	110°	
JD mid-time	r [AU]	Δ [AU]	α [°]	λ_c [μm]	FD [mJy]	σ [mJy]
2456022.55719	1.2368	0.4539	+50.4	70.0	9.47	1.80
"	"	"	"	160.0	<7.0	—

mospheric conditions and were not applied. Based on the quality of the stellar model for 66 Peg (Cohen et al. 1999), and uncertainties due to colour, aperture and atmosphere issues, we added a 5% error to account for the absolute flux calibration error in the various N-band filters. The updated flux densities, errors and observational circumstances are listed in Table 4.

2.4. Warm Spitzer observations in 2013

Ryugu was the target of an extensive photometric observation program (Mueller et al. 2012; 2013) in early 2013 using the Infrared Array Camera (IRAC, Fazio et al. 2004) onboard the Spitzer Space Telescope (Werner et al. 2004). The observations include ten "point-and-shoot" measurements consisting of short standard IRAC measurements that were spaced by several days up to a few weeks between January 20 and May 29, 2013, and two complete lightcurves, each using IRAC's channels 1 and 2 at nominal wavelengths of 3.550 μm and 4.493 μm, respectively⁴. The point-and-shoot observations were taken between 20th January and 29th May, 2013, covering a phase angle range between -54° and -102°. The lightcurve observations were taken on 10/11th February and 2nd May, 2013 at phase angles of -84° and -85°, respectively. Each lightcurve observation lasted approximately 8 hours, which is a little longer than a full rotation period of Ryugu. Observational details are given in Table 5.

IRAC's channels 1 and 2 observe the sky simultaneously, with non-overlapping field of views (FOV) that are a number of arc minutes offset from one another. As in previous IRAC observations of near-Earth objects (see, e.g. Trilling et al. 2010), we manually set up a dither pattern in which channels 1 and 2 alternate being on target (off-target frames are discarded in the data analysis). While this incurs additional overheads due to telescope slews, it enables quasi-simultaneous sampling between the two channels. The target was dithered on different parts of the FOV to minimize the impact of any pixel-to-pixel gain differences. The standard photometric measurements (point-and-shoot) took approximately 10 min each. For technical reasons, each of the two lightcurve observations (lc1a/b & lc2a/b) had to be split in two separate observations Astronomical Observation Requests ("AORs" in Spitzer terminology) that were scheduled back-to-back, with a gap of ~7.5 min between them. In the first lightcurve epoch, a 12 s frame time was used. Between the two AORs, there were 465 on-target frames per channel. The

⁴ The mnemonic Spitzer IRAC channel designations are 3.6 μm and 4.5 μm.

observation setup in the second lightcurve epoch was identical, except that two consecutive 6 s frames were used to avoid saturation. The Moving Object mode was used tracking at asteroid rates. Target movement during individual frames was at the sub-arcsecond level and hence much smaller than IRAC's pixel scale of 1.8''. Over the duration of a lightcurve, however, the target moved by tens of arc minutes, that is, several IRAC FOV widths.

The data reduction followed the method used in the Explore-NEOs program (Trilling et al. 2010). Briefly, a mosaic of the field is constructed from the data set itself and then subtracted from the individual Basic Calibrated Data (BCD) frames to mitigate contamination from background sources. Due to the short frame times, trailing of field stars during an individual BCD can be neglected. We were therefore able to generate a high signal-to-noise mosaic of the field. Aperture photometry was then performed on the background-subtracted frames. A small number of BCDs were rejected because the target was affected by bad IRAC pixels, cosmic-ray hits, or bright field stars. The derived IRAC fluxes and noise values from this Spitzer PID 90145 are given in the appendix (A, B) in Tables A.1, B.1, B.2, B.3, and B.4, including the two lightcurve measurement sequences in full-time resolution.

The measured IRAC fluxes account for the sum of sunlight reflected by the object and thermally emitted flux, integrated over the IRAC passbands. Due to the low albedo of our target combined with its low heliocentric distance, the reflected flux contribution is relatively small. We estimated that the reflected-light contributions are approximately 2-3% at 3.55 μm (approximately 10% at 3.1 μm where the bandpass opens) and well below 1% at 4.49 μm. We did not subtract these contributions, but consider it in the radiometric analysis in our thermophysical model setup which includes thermal emission and reflected light simultaneously. To obtain monochromatic flux densities at the channel 1&2 reference wavelengths, we have to colour-correct the thermal fluxes. Here, we used model calculations of the object's SED (reflected light and thermal emission) and combined it with the publically available IRAC spectral response tables⁵. The resulting colour-correction factors weakly depend on the selected object properties. We used a 6% albedo in combination with a thermal inertia of 200 J m⁻² s^{-0.5} K⁻¹ and obtained colour-correction factors⁶ of 1.09 (channel 1) and 1.04 (channel 2), with an estimated error of approximately 2% to cover object-SED and pass-

⁵ <http://irsa.ipac.caltech.edu/data/SPITZER/docs/-irac/calibrationfiles/spectralresponse/>; see also discussion in Hora et al. 2008

⁶ divide in-band thermal fluxes by correction factors to obtain monochromatic fluxes

band uncertainties, as well as differences in the observing geometry. In addition to the 2% error for colour correction, we also added a 5% error to account for limitations in the absolute flux calibration of the IRAC channels, diffuse straylight, moving target issues and possible other calibration changes during the warm part of the Spitzer mission⁷, such as intrapixel sensitivity variations or warm image features. The final colour-corrected flux densities and absolute flux errors are given in Table 5. For the two lightcurves, we averaged the observed fluxes (see Tables B.1, B.2, B.3, and B.4) over the rotation period of 7.63 h, colour-corrected the fluxes and added the calibration errors as for the point-and-shoot observations.

2.5. Additional thermal measurements

In addition, we also used Spitzer-IRS measurements. The single-epoch Spitzer-IRS spectrum was presented by Campins et al. (2009) and we used it in its calibrated full version and also in a rebinned version with 20 points over the entire wavelength range from 5.2 to 37.7 μm (see description in Müller et al. 2011a). The absolute IRS flux accuracy is given with 5-7% which is added quadratically to the uncertainties in the reduced spectrum. Later on, in Section 5.2.1 we also use the IRS spectrum without the absolute calibration error for comparing the measured SED slopes with TPM slopes.

3. Ground-based visual observations of 162173 Ryugu with GROND

The Gamma-Ray burst Optical-Near-ir Detector (GROND, Greiner et al. 2008) is mounted on the MPI 2.2m telescope at the ESO La Silla observatory (Chile). GROND observes in four optical- (g' , r' , i' , z') and three near-IR (J , H , K) filters, simultaneously. The observations of 162173 Ryugu were performed in pointing mode with four dithers carried out every minute to place the source again in the centre of the 5.4×5.4 arcmin² FOV of the optical Charge-Coupled Devices (CCDs).

A first short set of observations was taken on 27/28th May, 2012, for 2×4 min, followed by ≈ 5 hr coverage on 8th June 2012 (with a 1.5 hr gap in between) and another 3 hr the following night. Table 6 provides a list of observations taken including heliocentric distance r , observatory-centric distance Δ and the phase angle α .

The GROND data were reduced and analysed with the standard tools and methods described in Krühler et al. (2008). The g' , r' , i' photometry was obtained using aperture photometry with aperture sizes corresponding to 1.5'' (approximately $2 \times$ the width of the PSF) to include the complete flux of the slightly elongated source images (Ryugu was moving approximately 0.8'' during the ≈ 35 s integration times). The z , J , H , and K -band measurements were not used for the analysis due to the substantially lower S/N.

The photometry and photometric calibration of 162173 Ryugu was achieved as follows. First, the moving target was extracted from the list of detected sources for each band and filter by its observatory-centric position. For each sequence number in each observation ID we extracted the object's magnitude and its statistical photometric error for each of the four target dither positions. We additionally extracted several reference stars which were close to the path of Ryugu and similar in brightness (or brighter). As not every star was seen throughout the night (due to the rapid movement of Ryugu of around 100''/h which required

frequent re-pointing of the telescope), we selected several stars so that we had three to four stars at each given time. We monitored the magnitudes of these stars, calibrated against USNO (g' , r' , i'), in parallel to the object's magnitudes. This resulted in 1- σ accuracies of approximately 0.02 mag in the given bands. As the absolute photometric calibration of USNO is not very accurate, only the relative photometry is used in the remainder of the analysis. The results of the GROND lightcurve measurements (one value per TDP⁸, i.e. for each GROND pointing) are given in Tables C.1 and C.2 in the appendix. The magnitude errors include the photon noise (approximately 0.01-0.03 mag depending on the time of measurements during the nights) and the error from the corrections related to the multiple star measurements (typically well below 0.01 mag). There is also a flat-field error due to the varying position of Ryugu on the GROND camera (0.01 to 0.02 mag) which is difficult to quantify for an individual observation, but explains the scatter for some of the data points.

4. Searching for the spin-axis orientation

The standard lightcurve inversion technique (Kaasalainen & Torppa 2001; Kaasalainen et al. 2001) derives the asteroid's shape, sidereal rotation period and spin-axis direction from the observed lightcurves. Earlier work by Müller et al. (2011a), based on a smaller sample of lightcurve observations of Ryugu, found many solutions with different shapes, spin-orientations and rotation periods, all being compatible in the χ^2 -sense with the available visual data. This analysis was followed by using the derived solutions in the context of the available thermal data. The radiometric technique could eliminate wide ranges of solutions but did not lead to a unique spin-axis orientation. We repeated this procedure, now using many more lightcurve observations and additional thermal data points. However, the almost spherical shape and the insufficient quality of some data sets made this exercise very challenging and no unique solution was found. We therefore tried a different path.

4.1. Spherical shape model

Knowing that the observed lightcurve amplitudes are small (the amplitude is approximately 0.1 mag) we simply assumed a spherical shape model with the spin-axis orientation, size, albedo and thermal inertia as free parameters. Also, instead of using the visual lightcurves first, we started by using the thermal measurements. This approach worked very well in the case of (101955) Bennu where the radiometrically established spin-axis orientation (Müller et al. 2012) agreed within error bars with the radar derived value (Nolan et al. 2013). Furthermore, in the case of the very elongated object (25143) Itokawa, a careful analysis of thermal data in combination with a spherical shape model led to realistic predictions for the orientation of the object's spin vector within approximately 10° of the in-situ measured values (Müller et al. 2014).

The analysis was performed by means of a TPM code (Lagerros 1996; 1997; 1998). The target is described by a given size, shape, spin-state and albedo and placed at the true, epoch-specific observing and illumination geometry. The TPM considers a 1-d heat conduction into the surface with the thermal inertia Γ being the critical parameter. Surface roughness is also included, described by 'f' the fraction of the surface covered by spherical crater segments and ' ρ ', the r.m.s. of the surface slopes, connected to the crater width-to-depth ratio (Lagerros 1998). For

⁷ <http://irsa.ipac.caltech.edu/data/SPITZER/docs/irac/>

⁸ Telescope Dither Position

Table 7. Summary of general TPM input parameters and applied ranges.

Param.	Value/Range	Remarks
Γ	0...2500	[J m ⁻² s ^{-0.5} K ⁻¹], thermal inertia
ρ	0.0...0.9	r.m.s. of the surface slopes
f	0.6	surface fraction covered by craters
ϵ	0.9	emissivity
H_V -mag.	19.25 ± 0.03	[mag], Ishiguro et al. (2014)
G-slope	0.13 ± 0.02	Ishiguro et al. (2014)
shape	spherical shape	see Sect. 4.1
	convex shapes	see Sect. 4.2
spin-axis	4 π	see Sect. 4
P_{sid}	7.6312	[h], see Sect. 4.1
	free parameter	see Sect. 4.2

each surface facet, the energy balance between solar insolation, reflected light and thermal emission is treated individually. The reflected light contribution is calculated by multiplying the solar irradiance with the bidirectional reflectance and the transition phase between reflected light and thermal emission is estimated using Lambert's scattering law (Lagerros 1996 and references therein). We use the H-G system (Bowell et al. 1989) to describe the amount of reflected light. We used $H_V = 19.25 \pm 0.03$ mag and $G = 0.13 \pm 0.02$ which was derived from calibrated V-band observations covering a very wide phase angle range (Ishiguro et al. 2014). Table 7 summarises the general TPM settings for our radiometric analysis.

4.1.1. Using only mid-/far-IR thermal data

In the first step we used the above-mentioned thermal measurements by Herschel-PACS (Tbl. 2), Subaru-COMICS (Tbl. 4), AKARI, and Spitzer-IRS (see Müller et al. 2011a), but we excluded the Spitzer-IRAC measurements (Tbl. 5). The IRAC measurements are taken at shorter wavelengths (3.6 and 4.5 μm) where reflected light contributions might play a role. In addition, the individual short-wavelength (absolute) thermal fluxes are dominated by the hottest areas on the surface (related to local shape features near the sub-solar point), and global shape and spin properties are less relevant.

We used a spherical shape model with approximately 100 different spin axis orientations distributed over the entire 4 π solid angle. In a first round, we used a grid of pole directions with 30° steps, and later on we refined the steps around some of the promising pole directions (when the χ^2 -values were within 3 σ of an acceptable solution). This iterative approach worked well, knowing that the surface temperature distribution on a spherical shape model changes only gradually when changing the pole direction by one step. Size, albedo and thermal inertia are the dominating object properties when trying to reproduce the observed fluxes; the roughness has only a minor influence. We started by assuming a moderate surface roughness (r.m.s.-slopes of 0.2) to lower the number of free parameters in the first iteration.

For each value of the spin axis, we solved for the effective size and geometric albedo for a wide range of thermal inertias ranging from 0 (regolith with extremely low heat conductivity) to 2500 J m⁻² s^{-0.5} K⁻¹ (bare rock surface with very high conductivity). The results are shown in Figure 1 (top) with one curve per spin-axis orientation, each with a specific size/albedo solution as

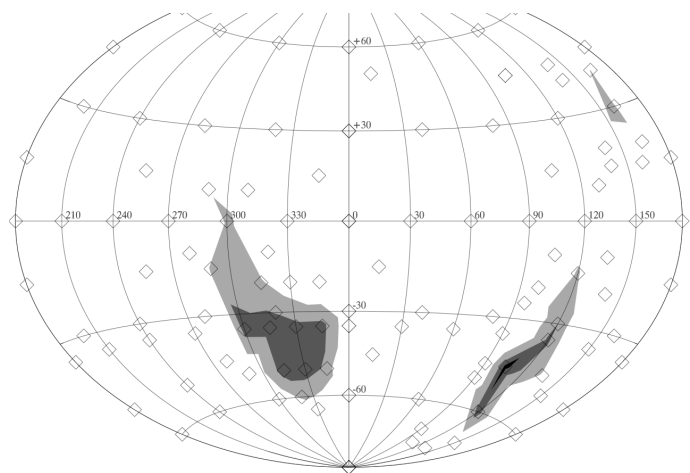
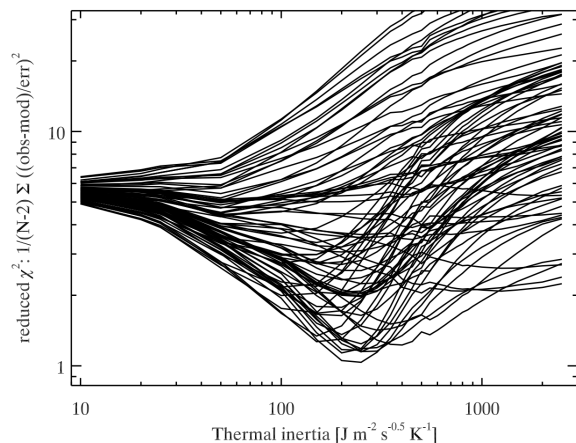


Fig. 1. χ^2 test for the complete set of spin-vector orientations and the full range of thermal inertias. Values close to 1.0 indicate acceptable solutions. Top: Reduced χ^2 values as a function of thermal inertia. Bottom: 1 σ - (dark grey), 2 σ - (intermediate grey), and 3 σ - (light grey) χ^2 values as a function of spin-axis ecliptic longitude and latitude in aitoff projection. The (λ ; β) ecliptic coordinates of all tested orientations are shown as diamonds.

a function of thermal inertia. Reduced χ^2 values close to 1.0 indicate a good fit to the thermal data set. In the bottom part of the figure we show the standard χ^2 values in the ecliptic longitude and latitude space: $\chi^2 = \Sigma((FD_{TPM} - FD_{Obs})/err_{Obs})^2$, with the confidence levels indicated by grey colours: 1- σ level agreement (dark grey) where $\chi^2 < \chi_{min}^2 + 1^2$, 2- σ level (intermediate grey) where $\chi^2 < \chi_{min}^2 + 2^2$, and 3- σ level (light grey) where $\chi^2 < \chi_{min}^2 + 3^2$. Many orientations of the spin axis can be excluded with very high probability; they simply do not allow us to explain all thermal measurements simultaneously, independent of the selected thermal inertia (and size/albedo). However there are still two remaining zones for the possible spin vector: (1) longitudes 90-130° and a wide range of latitudes from -15° to -70°; (2) longitudes 290-350° combined with latitudes +10° to -60°. At the 3- σ level there is even a third small zone at an approximate longitude 160° and latitude +30°. The true zones are probably slightly larger considering that we assumed a spherical shape and a fixed level of surface roughness.

4.1.2. Using Spitzer-IRAC averaged lightcurve measurements

Before investigating the full IRAC data set, we looked into the most crucial aspect for our spherical-shape analysis; namely the target’s flux increase between 10/11th Feb. and 2nd May, 2013, the epochs when full lightcurves were taken by Spitzer-IRAC. The flux increase is related to two effects: (i) The changed observing geometry: the Spitzer-centric distance decreased from approximately 0.23 AU in Feb. 2013 to approximately 0.11 AU in May 2013 (while the heliocentric distances and phase angles were very similar); (ii) The object moved on the sky by approximately 88° between February and May 2013, and depending on the orientation of the spin axis, the aspect angle (the angle under which the observer sees the rotation axis) was very different. The flux change between the two Spitzer lightcurve epochs is therefore very much related to the object’s spin-axis orientation. Table 5 contains details of these measurements.

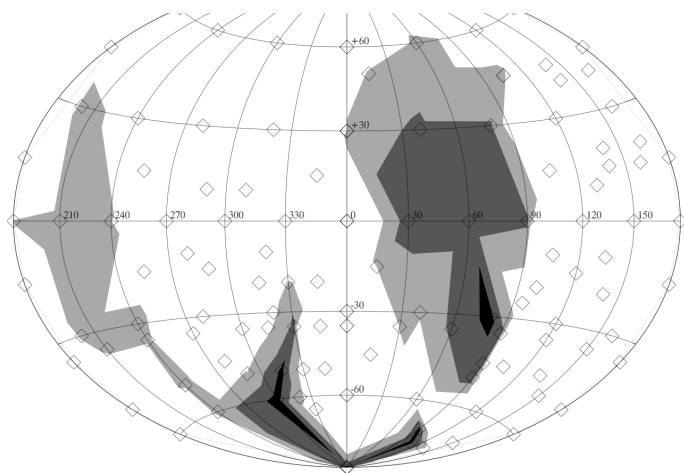


Fig. 2. Comparison between model flux ratios and the observed Spitzer-IRAC flux ratio of 3.6 ± 0.2 in the $(\lambda; \beta)$ -space. The grey zones indicate spin-axis orientations which can reproduce the observed flux ratio on a $1\text{-}\sigma$ (dark-grey), $2\text{-}\sigma$ (intermediate-grey), and $3\text{-}\sigma$ (light-grey) level.

We use the lightcurve-averaged observed fluxes to avoid shape effects in our search for the spin vector (see entries <lc1> and <lc2> in Tbl. 5). We also did not convert the observed in-band fluxes into monochromatic flux densities at the reference wavelength due to unknowns in the object’s SED at these short wavelengths where reflected light starts to play a role. The SED shape at wavelengths below $5\ \mu\text{m}$ is, in general, very sensitive to the highest surface temperatures and this depends on unknown surface structures, roughness and possibly also on material properties.

The flux changes between the two visits are independent of all corrections. The flux ratio between the second and the first epoch is $3.58 (\pm 0.1)$ in the $3.6\ \mu\text{m}$ band and $3.61 (\pm 0.05)$ in the $4.5\ \mu\text{m}$ band. For our calculations we used a conservative average flux ratio of 3.6 ± 0.2 , independent of wavelengths.

Starting out again with the spherical shape model, we determined the size, albedo and thermal inertia solution connected to the minima in the reduced- χ^2 curves, for each of the 100 spin orientations (top part of Fig. 1) to guarantee in each case the optimal solution with respect to our full thermal data set. Now we can predict the model fluxes and flux ratios for the two Spitzer epochs for each spin orientation (see Table 5). We compare the model flux ratios with the observed flux ratio of 3.6 ± 0.2 by calculating the χ^2 -values $((FD_{ep2}^{TPM}/FD_{ep1}^{TPM}) - 3.6)/0.2)^2$ and the

corresponding 1- , 2- , and $3\text{-}\sigma$ thresholds (see formula above). Figure 2 shows the result of this χ^2 -test on the basis of the observed IRAC flux ratio. Here again, large ranges of spin-axis orientations can be excluded because of a mismatch with the observed flux ratio. There remain, however, many possible pro- and retrograde solutions.

4.1.3. Summary spherical shape approach

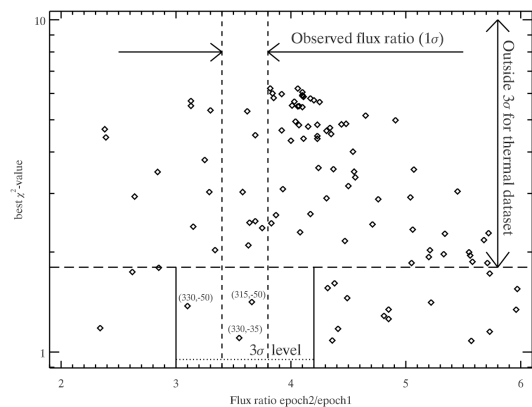


Fig. 3. Calculated flux ratios for the two IRAC epochs on 2nd May and 10/11th Feb, 2013, as a function of the minimum χ^2 values from Figure 1. The observed IRAC flux ratio of 3.6 ± 0.2 (and the $3\text{-}\sigma$ level) is indicated by vertical lines and the acceptance level from the analysis of the thermal data set is given by the dashed horizontal line.

Figure 3 shows the summary of both constraints with each spin-orientation represented by a diamond. The y-axis shows the values of the reduced χ^2 minima from Fig. 1 (top), the x-axis shows the corresponding model prediction for the IRAC flux ratio. The points below the horizontal long-dashed line show all solutions which are compatible (3σ) with the thermal data set, the vertical dashed lines indicate the observed flux ratio and the solid lines indicate the $3\text{-}\sigma$ range). There are only three solutions compatible with both constraints: $(\lambda; \beta)_{ecl} = (315^\circ, -50^\circ)$, $(330^\circ, -35^\circ)$, and $(330^\circ, -50^\circ)$, with the first two being within both $1\text{-}\sigma$ levels. Due to coarse sampling of the 4π space and the various assumptions for the shape and surface roughness, we estimated that the true spin-vector solution must lie somewhere in the range 310° to 335° in ecliptic longitude and -65° to -30° in ecliptic latitude. Our analysis from Sections 4.1.1 and 4.1.2 for this range of pole solutions points to a low-roughness surface (r.m.s. of surface slopes below 0.2) and thermal inertias of approximately $200\text{-}300\ \text{J m}^{-2} \text{s}^{-0.5} \text{K}^{-1}$, but still with significant uncertainties in size (approximately 815-900 m) and albedo (between 0.04 and 0.06).

4.2. Using thermal and visual-wavelength photometric data together

To confirm the results obtained by the method described in the previous section, we tried another independent approach to determine the spin axis orientation of Ryugu, using both photometric data and all thermal data together in one inversion procedure. The thermal data are the ones previously published and

presented in Section 2, the visual lightcurves are presented in M.-J. Kim et al. (in preparation) together with a set of ground-based observations taken with GROND mounted on the MPI 2.2m telescope at the ESO La Silla observatory (Chile) which is described in Section 3 and in the appendix C. The method is a modification of the standard lightcurve inversion of Kaasalainen et al. (2001) including also a thermophysical model. Its output is a convex shape model together with all relevant geometrical and physical parameters (spin axis direction, rotation period, size, thermal inertia of the surface, albedo and surface roughness) that best fit the lightcurves and thermal fluxes. It uses the Levenberg-Marquardt algorithm to minimize the χ^2 difference between the data and the model by optimising the model parameters. The total χ^2 of the fit is composed of two parts

$$\chi^2 = \chi_{\text{LC}}^2 + w \chi_{\text{IR}}^2, \quad (1)$$

where χ_{LC}^2 corresponds to the difference between the model and photometric data and χ_{IR}^2 corresponds to the difference between the model and thermal data. The relative weight w of one data source with respect to the other is set such that the best-fit model gives an acceptable fit to both data sets. Formally, the optimum weight can be found with the approach proposed by Kaasalainen (2011). Note that, overall, we use approximately 3100 data points from lightcurve measurements (Kim et al., in preparation, and appendix C) in addition to the large collection of thermal measurements (see Sect. 2), while the pole, rotation period, size, thermal inertia and shape are used as free parameters. For our calculations we used the rebinned Spitzer-IRS spectrum, 18 Subaru-COMICS measurements, 2 AKARI & 1 Herschel-PACS data points, as well as the 2 Spitzer-IRAC thermal lightcurves and the 10-epoch IRAC point-and-shoot sequence, with IRAC data always taken in two channels.

The thermo-physical part of the code is based on solving 1D heat conduction to get the temperature of each surface facet, for which the flux is computed. It is an independent implementation of the TPM code described in Sect. 4.1 based on the thermal model of Lagerros (1996; 1997; 1998). The hemispherical albedo needed for the boundary condition at the surface is computed in each step from the parameters of the Hapke's photometric model that is also used in the photometric part. This new method has been developed by Āurech et al. (2012) and tested on asteroid (21) Lutetia, as well as on several other asteroids. We describe the method and its results in detail in a separate paper (Āurech et al., in prep.).

The results for Ryugu are shown in Fig 4, where the fit to the lightcurves, thermal data and the combined total χ^2 is plotted for a grid of pole directions with a 5° step and the rotation period $P = 7.6300$ h. Because the model is rather flexible and the quality of the lightcurves is poor, there is no clear minimum in χ^2 that would define a unique spin direction. Moreover, even the sidereal rotation period cannot be determined unambiguously from the current data set. There are more possible values ($P = 7.6300, 7.6311, 7.6326$ h, for example) that give essentially the same fit to the data and very similar χ^2 maps for the pole direction. However, some solutions with low values of χ^2 are not correct in the physical sense; the model fits the data well, but the corresponding shape is too elongated along the rotation axis, which does not agree with the assumption of a relaxed rotation around the principal axis with the maximum inertia. Because the inversion algorithm works with the Gaussian image of the body (see Kaasalainen & Torppa 2001), the inertia tensor cannot be constrained during the shape optimisation. The alignment of rotation

and principal inertia axes has to be checked afterwards and unphysical models must be rejected. For each model, we computed the moment of inertia I_z corresponding to the rotation around the actual z axis and moment of inertia I_3 corresponding to the rotation along the shortest axis (minimum energy). We plot the ratio I_3/I_z for all poles in Fig. 5. The artificial boundary of 1.1 (based on our experience with models from lightcurves) divides those solutions that are formally acceptable ($I_3/I_z < 1.1$) from those that are not.

Another constraint we used was related to thermal inertia Γ of our models that is shown in Fig. 6. According to Campins et al. 2009, thermal inertia of Ryugu is higher than $150 \text{ J m}^{-2} \text{ s}^{-0.5} \text{ K}^{-1}$, which is also confirmed by our analysis in Section 5.2.1. Therefore, from all solutions in Fig. 4 (and also from similar maps for two other acceptable periods of 7.6311 and 7.6326 h), we selected only those that had $I_3/I_z < 1.1$ and $\Gamma > 150 \text{ J m}^{-2} \text{ s}^{-0.5} \text{ K}^{-1}$. These are shown in Fig. 7, where the blue areas show plausible pole solutions with low total χ^2 . Still the pole direction is not well defined.

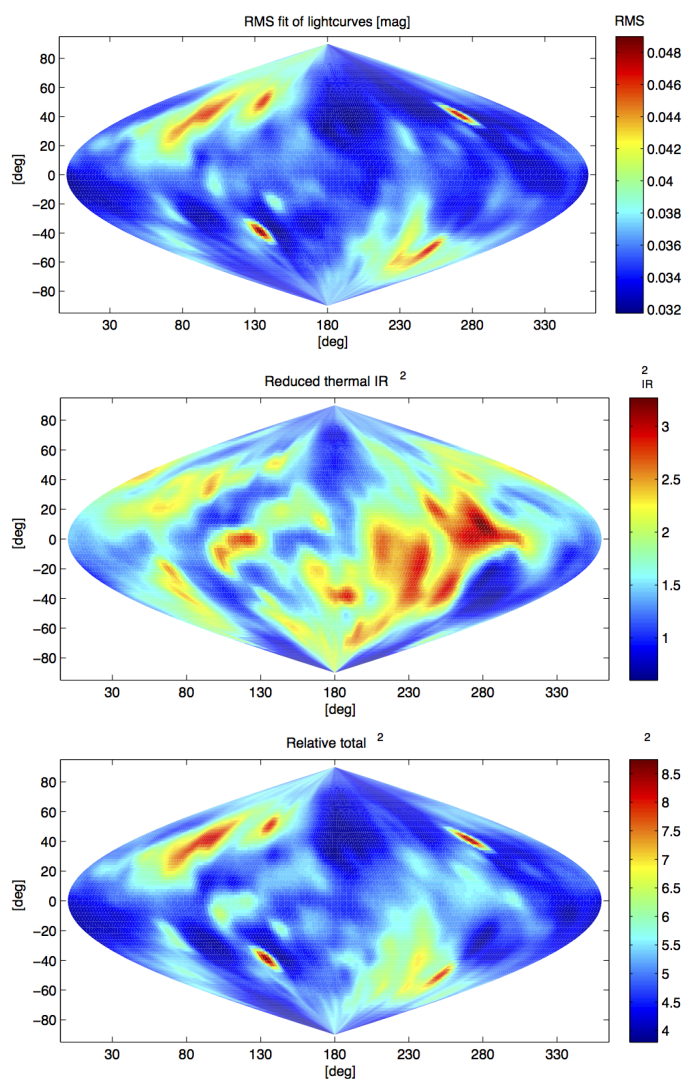


Fig. 4. The colour map of the goodness of fit for the lightcurves, thermal data and combined data for all possible orientations of the spin axis given in ecliptic coordinates (λ, β) . The top panel shows the rms residuals between the model and observed lightcurves, the middle plot shows the reduced χ^2 for the thermal data and the bottom plot shows the total χ^2 (Eq. 1).

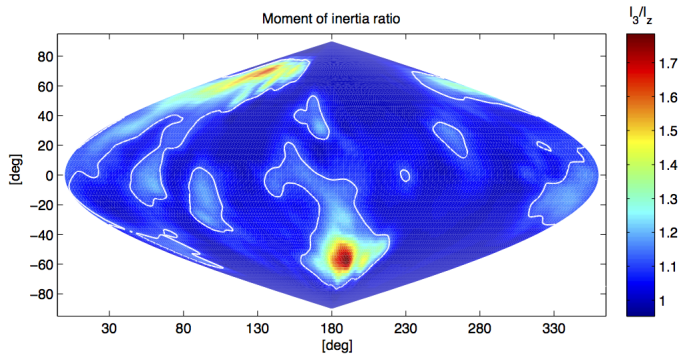


Fig. 5. The colour map of the ratio I_3/I_z for models corresponding to all possible orientations of the spin axis given in ecliptic coordinates (λ, β) . The white contour corresponds to the level 1.1.

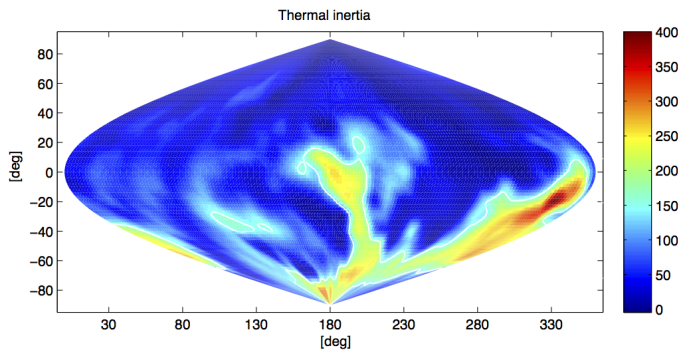


Fig. 6. The colour map of the thermal inertia Γ for models corresponding to all possible orientations of the spin axis given in ecliptic coordinates (λ, β) . The white contour corresponds to $\Gamma = 150 \text{ J m}^{-2} \text{ s}^{-0.5} \text{ K}^{-1}$.

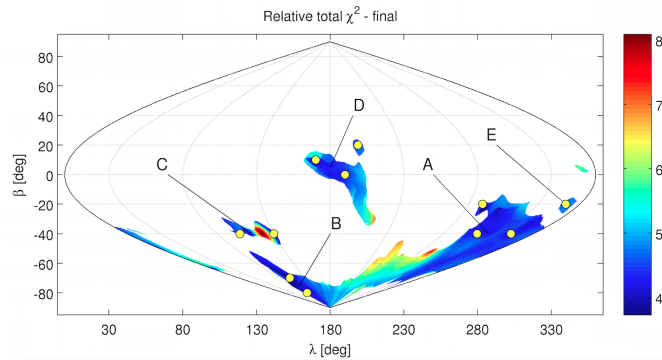


Fig. 7. The intersection between the total χ^2 colour maps (Fig. 4) for three possible rotation periods and the conditions $I_3/I_z < 1.1$ and $\Gamma > 150 \text{ J m}^{-2} \text{ s}^{-0.5} \text{ K}^{-1}$.

Because this convex model is more flexible than the spherical model from Sections 4.1.1 and 4.1.2, the range of possible pole directions is larger. Solutions with λ between 310 and 340° and $\beta \sim -40^\circ$ (denoted A in Fig. 7) are preferred because they not only provide the lowest χ^2 but are also stable against the limit of inertia ratio, the minimum value of Γ , particular value of the weight w in Eq. (1) and the resolution of the shape model. Moreover, they show no systematic trends in the distribution of residuals for the fit of thermal data and are also consistent with the results of the previous section. The formally best-fit model for period $P = 7.6311 \text{ h}$ has the pole direction $(340^\circ, -40^\circ)$, a volume-equivalent diameter of 853 m , a surface-equivalent diameter of

862 m , a thermal inertia of $220 \text{ J m}^{-2} \text{ s}^{-0.5} \text{ K}^{-1}$ and a very smooth surface (assuming no surface roughness in the model setup). The corresponding shape model is shown in Fig. 8 and the synthetic lightcurves produced by this model are compared with the observed lightcurves in Fig. 9.

The other formally possible pole directions correspond to other blue ‘islands’ (denoted A, B, C, D, E) in Fig. 7 with the approximate pole coordinates B: $(100^\circ, -70^\circ)$, C: $(100^\circ, -40^\circ)$, D: $(180^\circ, 0^\circ)$, and E: $(350^\circ, -20^\circ)$ (see Table 8).

Table 8. Summary of possible pole solutions in ecliptic coordinates (see Fig. 7) from our analysis of the combined visual and thermal data set. Zone ‘A’ is our preferred solution because this zone is connected to the lowest χ^2 and stable against the limit of inertia ratio, the minimum value of Γ , and different resolutions of the shape model (see also Section 4.2).

ID	Pole solution λ [$^\circ$]	β [$^\circ$]	P_{sid} [h]	Zone
1	290	-20	7.63108	A
2	340	-40	7.63109	A
3	310	-40	7.63001	A
4	100	-70	7.63254	B
5	90	-80	7.62997	B
6	130	-40	7.63256	C
7	100	-40	7.63005	C
8	170	10	7.63123	D
9	190	0	7.63001	D
10	200	20	7.63001	D
11	350	-20	7.63256	E

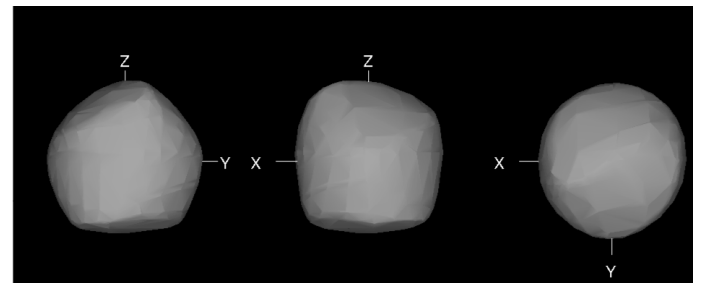


Fig. 8. The formally best-fit shape model of Ryugu for pole direction $(340^\circ, -40^\circ)$.

5. Discussion and final thermophysical model analysis

5.1. Analysis of previously published solutions

Campins et al. (2009) analysed a single-epoch IRS measurement and found a thermal inertia of $700 \pm 200 \text{ J m}^{-2} \text{ s}^{-0.5} \text{ K}^{-1}$ under the assumption of the published spin-axis orientation by Abe et al. (2008). They also investigated the reliability of the IRS data and found a rigorous lower limit of $150 \text{ J m}^{-2} \text{ s}^{-0.5} \text{ K}^{-1}$ for an extreme case of an equatorial retrograde geometry. We tested the Campins et al. (2009) solution ($\Gamma = 700 \pm 200 \text{ J m}^{-2} \text{ s}^{-0.5} \text{ K}^{-1}$, $D_{eff} = 0.90 \pm 0.14 \text{ km}$, $p_V = 0.07 \pm 0.01$, spherical shape, spin axis with $(\lambda, \beta)_{ecl} = (331^\circ, +20^\circ)$, $P_{sid} = 7.6272 \text{ h}$) against our

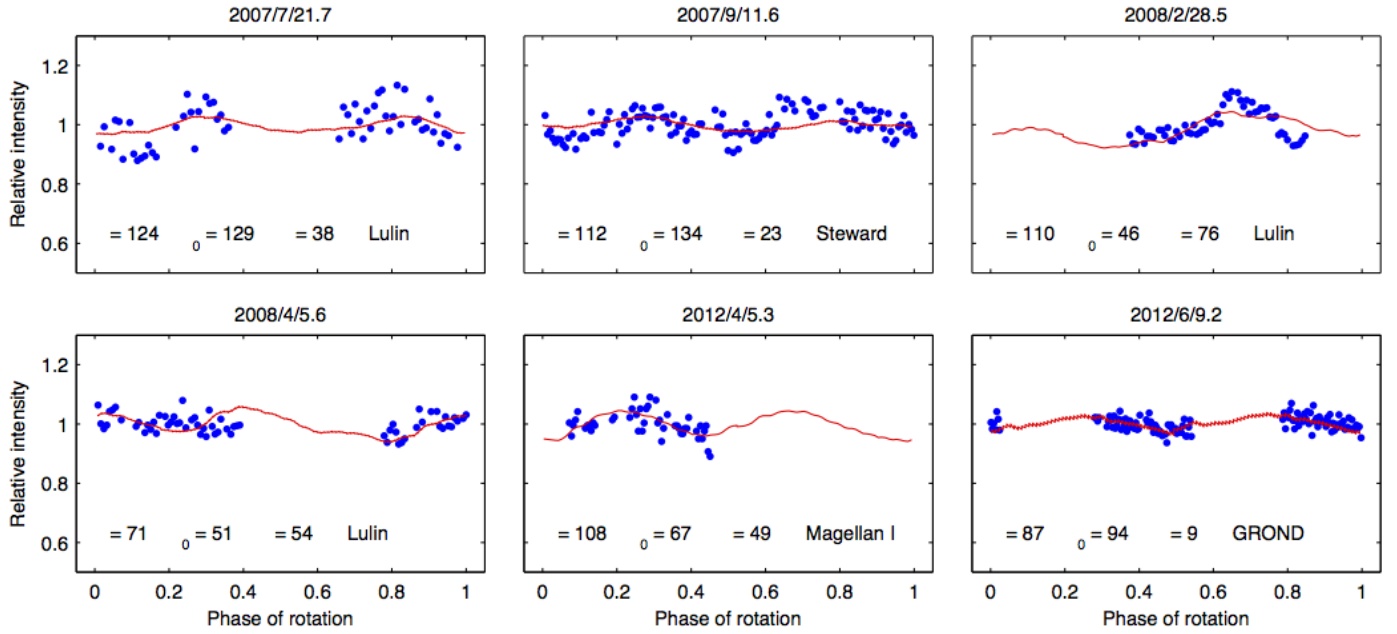


Fig. 9. Comparison between the model (red curves) and the data (points) for a subset of visual lightcurves. The viewing and illumination geometry for the corresponding pole ($340^\circ, -40^\circ$) is given by the latitude of sub-Earth point θ , latitude of the subsolar point θ_0 , and the solar phase angle α .

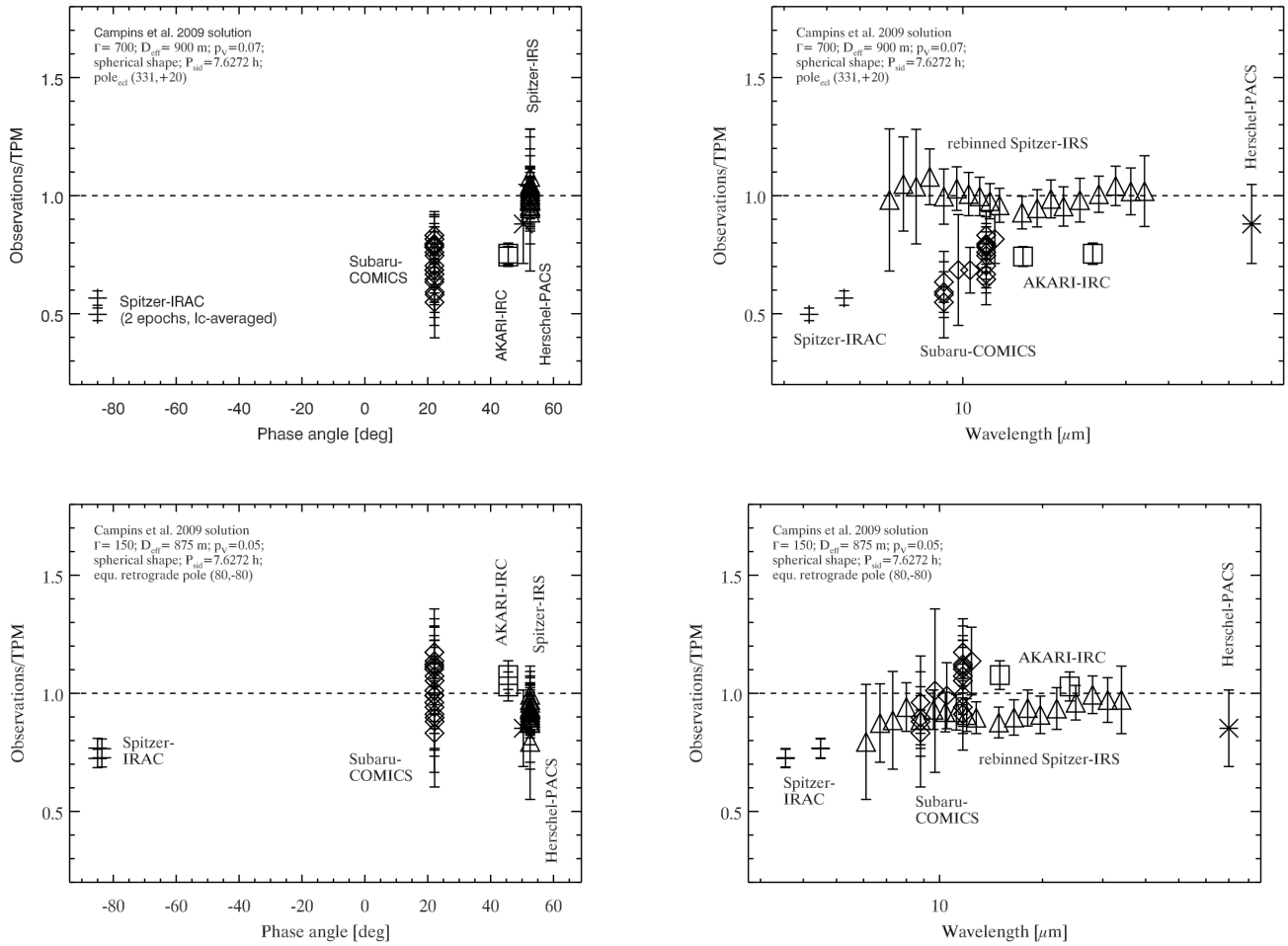


Fig. 10. Test of the Campins et al. (2009) solutions against our large thermal data set. Top left: Observation-to-TPM flux ratios as a function of phase angle; top right: as a function of wavelength; bottom left/right: same as top figure, but now calculated for the lower thermal inertia limit of $150 \text{ J m}^{-2} \text{ s}^{-0.5} \text{ K}^{-1}$ and the extreme case of an equatorial retrograde geometry (at the time of IRS observations and as seen from Spitzer).

thermal data set. Their solution explains the Spitzer-IRS measurements very well, with observation-to-model flux ratios close to one (see Fig. 10 top left/right), confirming the Campins et al. (2009) analysis. However, this solution fails to reproduce measurements at other phase angles. The high thermal inertia of $700 \text{ J m}^{-2} \text{ s}^{-0.5} \text{ K}^{-1}$ (in combination with the spin-axis orientation) leads to model predictions which are up to a factor of two higher than the measurements, with the largest offsets being connected to the before-opposition Spitzer-IRAC measurements. Using the limiting thermal inertia of $150 \text{ J m}^{-2} \text{ s}^{-0.5} \text{ K}^{-1}$ in combination with the extreme case of an equatorial retrograde geometry⁹ helps to explain part of the phase-angle-dependent offsets seen before (in combination with a radiometrically optimised size and albedo), but overestimates the IRAC lightcurves by approximately 25% and also introduces trends with wavelengths and phase angle in the ratio plots (Fig. 10 bottom left/right). We tested the full range of thermal inertias from 0-2500 $\text{J m}^{-2} \text{ s}^{-0.5} \text{ K}^{-1}$ for smooth and rough surfaces, but it was not possible to simultaneously explain all thermal measurements with either of these two spin-axis orientations. The remaining offsets are too big to be explained by shape effects without violating the constraints from the shallow visual lightcurves. The analysis of the Campins et al. (2009) solutions in the context of our much larger data set shows that (i) the high thermal inertia of $700 \text{ J m}^{-2} \text{ s}^{-0.5} \text{ K}^{-1}$ in combination with the spin axis by Abe et al. 2008) is not correct; (ii) the low thermal inertia of $150 \text{ J m}^{-2} \text{ s}^{-0.5} \text{ K}^{-1}$ in combination with an extreme case of an equatorial retrograde geometry is also problematic; (iii) the thermal data include crucial information about thermal inertia and the orientation of the spin axis; (iv) a single-epoch measurement, even if covering a wide wavelength range, is not sufficient to determine the object's thermal inertia; (v) offsets and trends between measurements and model predictions are clearly connected to incorrect assumptions in the model surface temperature distribution and not due to shape effects which could possibly explain offsets of 10%, but not the huge discrepancies seen in Fig. 10.

It is also worth taking a closer look at the three proposed solutions by Müller et al. (2011a). Here, the authors used more complex shapes, but their thermal data were limited to a phase angle range between $+20^\circ$ and $+55^\circ$ and the focus of the TPM analysis was on high-roughness surfaces. We tested all three shape-spin settings against our much larger thermal data set (including the IRAC point-and-shoot measurements), and now considering much smoother surfaces with r.m.s. surface slopes below 0.4. The calculations show the following: (i) all solutions seem to point to a much smoother surface than what was assumed in Müller et al. (2011a); (ii) their best solution $(\lambda, \beta) = (73.1^\circ, -62.3^\circ)$ in ecliptic coordinates leads to a thermal inertia of $200 \text{ J m}^{-2} \text{ s}^{-0.5} \text{ K}^{-1}$, and their solutions #2 and #3 would require lower thermal inertias below the Campins et al. limit of $150 \text{ J m}^{-2} \text{ s}^{-0.5} \text{ K}^{-1}$; (iii) solution #1 is close to our solutions in zone B (see Fig. 7 and Table 8) and explains most of the observational data within the given observational error bars. Only the PACS measurement and one of the IRAC lightcurve measurements are off by approximately 15-20%. This model also fails to explain part of the IRAC point-and-shoot sequence and produces observation-to-model flux ratios ranging from 0.78 to 1.55, some ratios even being well outside the $3\text{-}\sigma$ error bars. Interestingly, the point-and-shoot measurements in early 2013, when the phase

⁹ The extreme case of an equatorial retrograde geometry at the time of IRS observations and as seen from Spitzer corresponds to a spin-axis orientation of $(\lambda, \beta) = (80^\circ, -80^\circ)$.

angle was changing from -70° to -90° , are nicely matched, while some of the measured fluxes in May 2013 are up to 55% higher than the corresponding model predictions. In this time period, the phase angle was in the range -90° to -55° and the object had its closest approach to Spitzer (≈ 0.11 AU). Overall, solution #1 from Müller et al. (2011a) might still be acceptable from a statistical point of view (depending on the weight of the short-wavelength IRAC data in the radiometric analysis), but the mismatch to some IRAC measurements is obvious and we exclude that solution.

Yu et al. (2014) calculated a shape solution from MPC (Minor Planet Center) lightcurves, but their shape solution is not publically available. Looking at the MPC data, we doubt that a reliable shape can be reconstructed for the existing data. Also, the effective diameter of 1.13 ± 0.03 km ($p_V = 0.042 \pm 0.003$) is unrealistically large. Using the Yu et al. (2014) solution (in combination with a spherical shape) produces observation-to-model flux ratios in the range 0.43 to 0.88, that is, the model predictions are far too high.

5.2. New solutions and constraints on Ryugu's properties

5.2.1. Thermal inertia

The χ^2 analysis in the sections 4.1 and 4.2 point towards a pole direction close to $(310^\circ, -40^\circ)$, but it cannot completely rule out other solutions from a statistical point of view. This can also be seen in Fig. 11 where we show χ^2 curves as a function of thermal inertia for all remaining 11 shape and spin-pole solutions (Tbl. 8). The corresponding spherical shape solutions are shown as dashed lines. The most striking thing is that the lowest χ^2 values are all connected to thermal inertias of $200\text{--}300 \text{ J m}^{-2} \text{ s}^{-0.5} \text{ K}^{-1}$. There is another group of solutions with higher χ^2 values close to our thermal-inertia boundary of $150 \text{ J m}^{-2} \text{ s}^{-0.5} \text{ K}^{-1}$ (see analysis by Campins et al. (2009) of the Spitzer-IRS data), but no acceptable solutions anymore at Itokawa-like and higher values for the thermal inertia.

Our combined thermal data set, including the IRAC measurements, constrains the thermal inertia very well: we can confirm the thermal-inertia boundary of $150 \text{ J m}^{-2} \text{ s}^{-0.5} \text{ K}^{-1}$ (see analysis by Campins et al. (2009)) and starting at approximately $300 \text{ J m}^{-2} \text{ s}^{-0.5} \text{ K}^{-1}$ the models cannot explain the IRAC measurement sequences anymore.

5.2.2. Surface roughness

The statistical analysis in Section 4.2 led to a formally best solution for smooth surfaces. If we introduce roughness at a low level, we still find the best solutions connected to zone A, but now the best spin pole seems to move towards a higher longitude approaching the solution at $(340^\circ, -40^\circ)$. However, as soon as the r.m.s. of the surface slopes goes above 0.1 there are problems in fitting the IRAC point-and-shoot sequence, and also in fitting the two IRAC thermal lightcurves. Overall, higher levels of roughness are connected to size-albedo solutions with higher thermal inertias and vice versa. This degeneracy problem is present in most radiometric solutions (see also Rozitis & Green 2011 for a discussion on the degeneracy between roughness and thermal inertia), but here the low-roughness solutions are clearly favoured.

5.2.3. Size and albedo

Radiometric size and albedo constraints depend heavily on the shape-spin solution. In the central part of zone A (solution #2 in Table 8) we find sizes (of an equal volume sphere) of 850 to 880 m, and albedos of 0.044 to 0.050 (connected to $H_V = 19.25 \pm 0.03$ mag). Including the zone-A boundaries and considering the full thermal inertia and roughness range, as well as the corresponding shape solutions, we estimate a size range of approximately 810 to 900 m (of an equal-volume sphere) and geometric V-band albedos of approximately 0.042 to 0.055. However, all the solutions (#1 and #3 in Table 8) have issues with fitting part of the thermal data (see Section 5) and we restrict our size-albedo values to solution #2 in the central zone A.

5.2.4. Grain sizes

We use a well-established method (Gundlach & Blum 2013) to determine the grain size of the surface regolith of Ryugu. First, the thermal inertia Γ can be translated into a possible range of thermal conductivities λ with

$$\lambda = \frac{\Gamma^2}{\phi \rho c}, \quad (2)$$

where c is the specific heat capacity, ρ the material density, and ϕ the regolith volume-filling factor, which is typically unknown. This last parameter is varied between 0.6 (close to the densest packing or "random close pack (RCP)" of equal-sized particles) and 0.1 (extremely fluffy packing or "random ballistic deposition (RBD)", plausible only for small regolith particles where the van-der-Waals forces are larger than local gravity). For the calculation, we used the CM2 meteoritic sample properties from Opeil et al. (2010), with a density $\rho = 1700 \text{ kg m}^{-3}$, and a specific heat capacity of the regolith particles $c = 500 \text{ J kg}^{-1} \text{ K}^{-1}$. This leads to heat conductivities λ in the range $0.1 \text{ W K}^{-1} \text{ m}^{-1}$ (average thermal inertia combined with the highest volume-filling factor) to $0.6 \text{ W K}^{-1} \text{ m}^{-1}$ assuming the lowest filling factor (also considering the full thermal inertia range would result in a λ range of 0.04 to $1.06 \text{ W K}^{-1} \text{ m}^{-1}$).

We combine this information with the heat conductivity model by Gundlach & Blum (2013), again by using properties of CM2 meteorites, to estimate possible grain sizes on the surface. First, we calculated maximum surface temperatures in the range ≈ 320 to 375 K, considering the derived object properties and heliocentric distances (r_{helio} : 1.00 - 1.41 AU) of our observational (thermal) data set. At the object's semi-major axis distance ($a = 1.18$ AU) we find a reference maximum temperature of 350 K. It is worth noting that changing the surface temperature by a few tens of degrees does not significantly affect the results. In a second step, we determine the mean free path of the photons, the Hertzian dilution factor for granular packing for the specified regolith volume-filling factors. Our estimated grain sizes are in the range 1 to 10 mm, in excellent agreement with independent calculations by Gundlach (priv. communications) which led to 0.7 to approximately 7 mm grain sizes. We note that our value is different than values given in Gundlach & Blum (2013), mainly due to different assumptions for the thermal inertia. At the derived grain-size level, the heat transport on the surface is still dominated by radiation, with increasing heat conduction for lower thermal inertias.

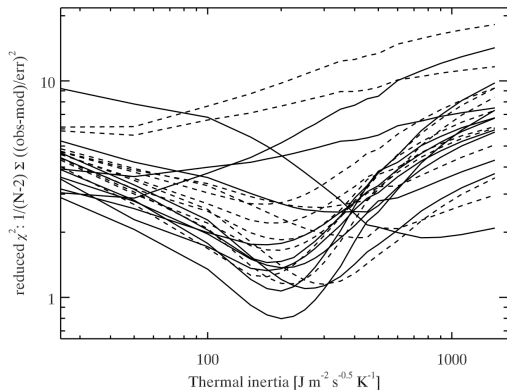


Fig. 11. Reduced χ^2 values as a function of thermal inertia for all 11 shape and spin-pole solutions. True shape solutions are shown as solid lines, spherical shapes as dashed lines. Acceptable solutions should have reduced χ^2 values close to 1.

5.2.5. Reference solution

Figures 12, 13, 15, and 14 inform us on the quality of our TPM predictions and the thermal IR data, in combination with wavelengths, phase angle and time of the individual measurements. For these figures we calculated the TPM predictions for each data point using the true observing and illumination geometry as seen from the specific observatory. The TPM fluxes are used in terms of absolute times and absolute fluxes; **no shifting or scaling was applied**. The model has the following settings:

- shape solution with $(\lambda, \beta) = (340^\circ, -40^\circ)$ in ecliptic coordinates; $P_{sid} = 7.63109$ h (#2 in Tbl. 8) from inversion technique using visual and thermal lightcurves and infrared photometric data points
- thermal inertia (top layer) of $200 \text{ J m}^{-2} \text{ s}^{-0.5} \text{ K}^{-1}$
- low surface roughness with r.m.s. of surface slopes of 0.05
- size (of an equal-volume sphere): 856 m
- geometric V-band albedo: 0.049 (connected to $H_V = 19.25$ mag)
- emissivity of 0.9

This TPM solution matches the different thermal observational data sets very well over wide ranges of phase angles, times, wavelengths and rotational phases. For the IRAC data (very short thermal wavelengths at the Wien-part of the SED) there are still small residuals, but here individual shape facets and local temperature anomalies can easily change the total fluxes and significantly influence the interpretation. At longer wavelengths, that is, in the Rayleigh-Jeans part of the spectrum, these small-scale shape and temperature features are less relevant. Here, the shape of the SED is connected to the disk-averaged temperature on the surface. The observed long-wavelength fluxes are therefore crucial for the determination of the object's size.

The observation-to-model plots in Figure 12 are very sensitive to changes in thermal inertia. Smaller thermal inertias lead to

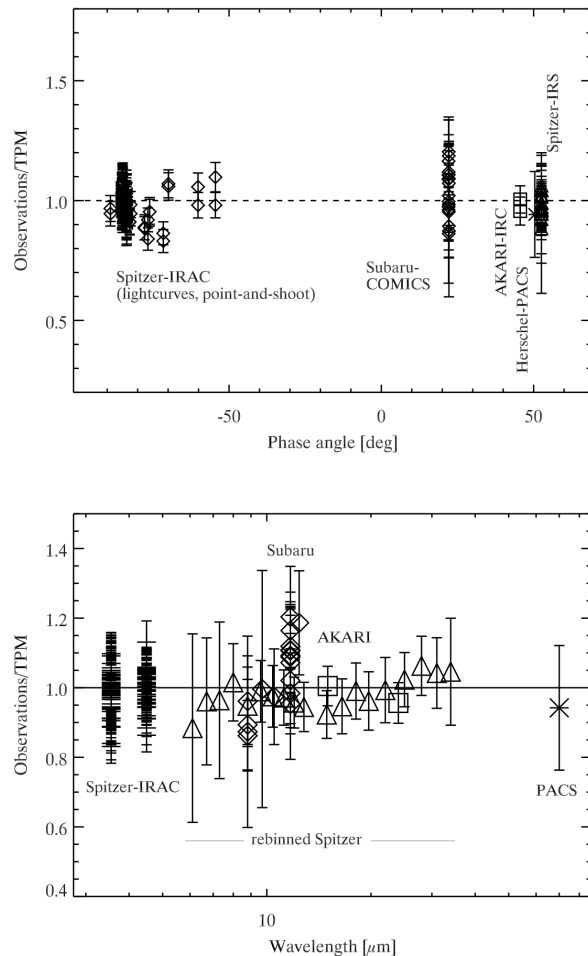


Fig. 12. All thermal observations divided by the corresponding TPM prediction based on solution #2 in Tbl. 8 as a function of phase angle (top), and as a function of wavelengths (bottom). No trend in observation-to-model flux ratios is visible over the very wide phase angle range from -89° to $+53^\circ$, nor over the wide range of wavelengths from 3.55 to $70 \mu\text{m}$. The rebinned IRS data are shown as triangles together with the absolute flux error of each individual data point.

a peaked temperature distribution (close to the sub-solar point) and the corresponding disk-integrated object flux is dominated by the hottest surface temperature; at least at short wavelengths below $5 \mu\text{m}$. Larger thermal inertias ‘transport’ the surface heat to the ‘evening’ parts of the surface which are not directly illuminated by the Sun. This redistribution leads to a slightly different shape of the spectral energy distribution since the warm regions at the evening terminator contribute noticeably to the total flux. As a result, the slope in observation-to-model flux ratios changes (best visible in Fig. 10, right side).

The difference between a warm evening side and a cold morning side is largest for large phase angles and at wavelengths close to or beyond the thermal emission peak at approximately $20 \mu\text{m}$ (see also figures and discussion in Müller 2002). Our thermal data set has observations taken before and after opposition, covering a wide range of phase angles, but the data are very diverse in wavelength and quality. The Spitzer IRAC data are all taken before opposition (negative phase angles, leading the Sun) and, in addition, these very short wavelengths are less sensitive to the morning-evening effects. All crucial data sets (AKARI, Subaru, Herschel) for constraining the thermal inertia via before-

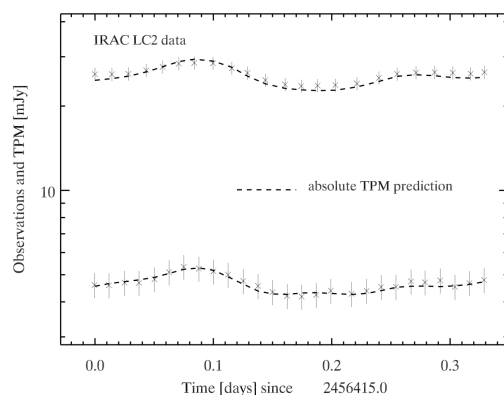
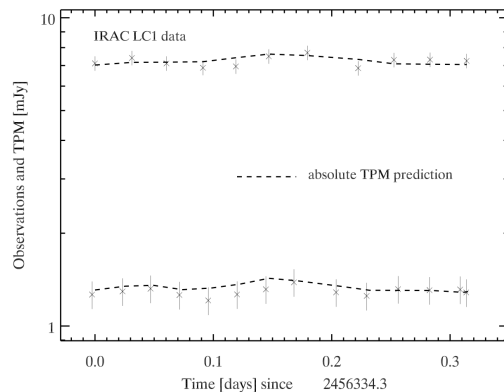
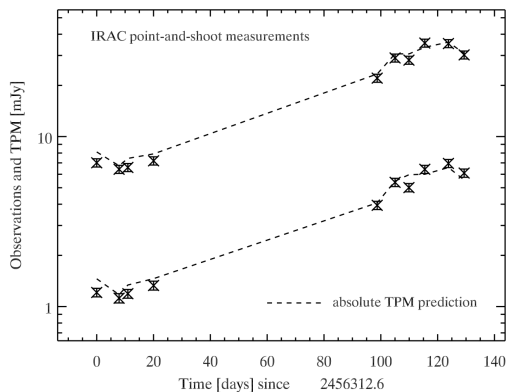


Fig. 13. Absolutely calibrated Spitzer-IRAC point-and-shoot fluxes at 3.550 and 4.493 μm taken between 20th Jan, and 30th May, 2013 (phase angles go from -71.6° to -88.9° and back to -54.5° during that period). The absolute TPM predictions (#2 n Tbl. 8) for both channels are shown as dashed lines.

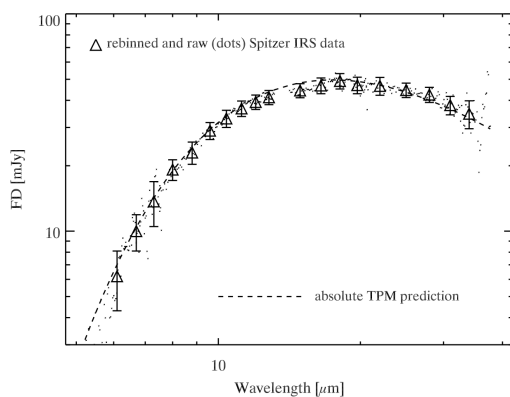


Fig. 14. The absolutely calibrated Spitzer-IRS spectrum from 2nd May, 2008 (see Campins et al. 2009), rebinned data are shown as triangles, the full data set as dots. The absolute TPM prediction (#2 n Tbl. 8) is shown as a dashed line.

after-opposition asymmetries are taken either at a very limited phase angle range (AKARI-IRC, Herschel-PACS) or have substantial error bars (Subaru-COMICS, Herschel-PACS).

The most direct thermal inertia influence can be seen in the Spitzer-IRS spectrum (see Fig 10, right side). The ratios between observed fluxes and the corresponding model prediction show a clear trend with wavelengths at low (and also at high) values of thermal inertia. The mismatch between observed and modeled fluxes is evident, and would be even larger in cases of higher thermal inertias. From a statistical point of view, both cases are still acceptable, but there are two reasons why we have higher confidence in #2 of Table 8 which is connected to a thermal inertia of around $200 \text{ J m}^{-2} \text{ s}^{-0.5} \text{ K}^{-1}$: (1) TPM predictions with lower or higher thermal inertias produce wavelength-dependent ratios increasing or decreasing with wavelength, respectively; these trends can be attributed to unrealistic model temperature

distributions on the surface; (2) For a comparison of model SED slopes with the observed IRS slope, it is more appropriate to use only the IRS measurement errors without adding an absolute calibration error. In this case, the low/high thermal inertia trends are statistically significant with many flux ratios at short and long wavelengths being outside the 3-sigma limit. However, for a realistic comparison with all other data sets we also used absolute flux errors for IRS data in Figs. 10, 12, and 14.

6. Conclusions

Despite our extensive experience in reconstructing rotational and physical properties of many small bodies and the large observational data set for Ryugu, this case remains challenging. The visual lightcurves have very low amplitudes and the data quality is not sufficient to find unique shape and spin properties in a standard way by lightcurve inversion techniques.

We have collected all available data sets, published and unpublished, and obtained a large data set of new visual and thermal measurements from ground and space, including Herschel, Spitzer, and AKARI measurements, with multi-epoch, multi-

phase angle and wavelength coverage. We also re-reduced previously published data (Subaru, AKARI) with improved methods.

We combined all data and analysed them using different methods and thermophysical model codes with the goal being to determine the object's size, albedo, shape, surface, thermal and spin properties. In addition to standard (visual) lightcurve inversion techniques, we applied TPM radiometric techniques assuming spherical and more complex shapes, and also a new radiometric-inversion technique using all data simultaneously. Our results are thus summarised: This C-class asteroid has a retrograde rotation with the most likely axis orientation of $(\lambda, \beta)_{ecl} = (340^\circ, -40^\circ)$, a rotation period of $P_{sid} = 7.63109$ h and a very low surface roughness (r.m.s. of surface slopes < 0.1). The object's spin-axis orientation has an obliquity of 136° with respect to Ryugu's orbital plane normal (full possible range: 114° to 136°). We find a thermal inertia of the top-surface layer of $150 - 300 \text{ J m}^{-2} \text{ s}^{-0.5} \text{ K}^{-1}$, and, based on estimated heat conductivities in the range 0.1 to $0.6 \text{ W K}^{-1} \text{ m}^{-1}$, we find grain sizes of $\approx 1\text{-}10$ mm on the top-layer surface. We derived a radiometric size (of an equal-volume sphere) of approximately 850 to 880 m (connected to the above rotational and thermal properties). Considering also the less-likely solutions from zones B and C in Table 8 would widen the size range to approximately 810 to 905 m. The convex shape model has approximate axis ratios of $a/b = 1.025$ and $b/c = 1.014$. Some of the solutions in Table 8 have more elongated shapes with a/b rising to approximately 1.06 , and b/c axis ratios ranging from 1.01 to 1.07 ; one of the solutions (#5 in Table 8) shows a more extreme b/c ratio of 1.21 . Using an absolute magnitude in V-band of $H_V = 19.25 \pm 0.03$ mag we find a geometric V-band albedo of $p_V = 0.044\text{-}0.050$. Less probably, solutions from Table 8 would result in an albedo maximum of 0.06 . A radiometric analysis using a simple spherical shape points to a very similar spin-vector solution lying somewhere in the range 310° to 335° in ecliptic longitude and -65° to -30° in ecliptic latitude, connected to a low-roughness surface (r.m.s. of surface slopes below 0.2), thermal inertias of approximately 200 to $300 \text{ J m}^{-2} \text{ s}^{-0.5} \text{ K}^{-1}$, but still with significant uncertainties in size (approximately $815\text{-}900$ m) and albedo (between 0.04 and 0.06), but in excellent agreement with our final solution. Automatic procedures using radiometric and lightcurve inversion techniques simultaneously led to a range of possible spin solutions (from the statistical point of view), grouped into five different zones (see Fig. 7). A more careful (manual) testing of all solutions within the five zones was required to find the most likely axis orientation in the context of our large, but complex thermal data set.

Our analysis shows that thermal data can help to reconstruct an object's rotational properties, in addition to its physical and thermal characteristics. But the Ryugu case also shows that: (i) high-quality multi-aspect visual lightcurves are crucial for reconstructing shape and spin properties, and even more for cases with low-amplitude lightcurves; (ii) thermal data can help to reconstruct the spin properties, also in cases of low-amplitude lightcurve objects; (iii) there are many ways of combining visual (originating from the illuminated surface only) and thermal data (related to the warm surface areas) in a single inversion technique, and the outcome depends strongly on the quality of individual data sets and the weights given to each data set; (iv) thermal data are very important for constraining size, albedo, and thermal inertia, but one must consider the degeneracy between thermal inertia and surface roughness: often low-roughness combined with low-inertia solutions fit the data equally well as high-roughness combined with high-inertia settings; (v) thermal data also carry information about the object's spin-axis orientation,

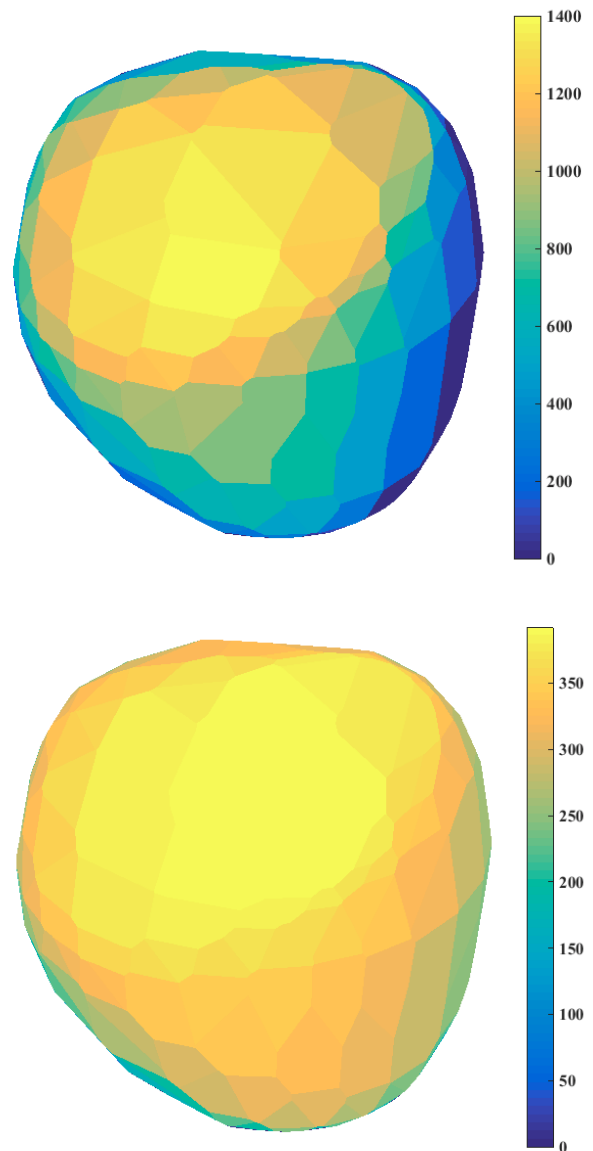


Fig. 16. Ryugu as seen from Earth on 1st July, 2018, close to the arrival time of the Hayabusa-2 mission at the asteroid ($r=0.988$ AU, $\Delta=1.903$ AU, $\alpha=18.6^\circ$), calculated using our reference shape, spin (#2 in Tbl. 8), size, thermal solution, with the z-axis pointing in the direction of the spin axis (along the insolation/temperature colour bars). Top: Solar insolation in W/m^2 , with the sub-solar point located at the peak insolation. Bottom: The TPM-calculated temperatures (in Kelvin).

but the interpretation is not straight forward: first of all, shape features can be misleading, secondly, short-wavelength fluxes (such as the short-wavelength Spitzer-IRAC data) are originating from the hottest terrains on the surface and global shape and spin properties have weaker influences; (vi) long-wavelength thermal data (beyond the thermal emission peak) are crucial for constraining size, albedo and thermal inertia, and they are important for reconstructing spin properties (if error bars are not too large); (vii) single-epoch thermal observations, even in cases with a full thermal emission spectrum as obtained by Spitzer-IRS, can lead to incorrect thermal inertias.

Our favoured solution (#2 in Tbl. 8) can now be used to make visual and thermal predictions for future observations. This solution is also the "design reference model" for the preparation and

conduction of the Hayabusa2 mission. Figure 16 shows the thermal picture of Ryugu close to the arrival time of the Hayabusa-2 mission in July 2018.

Acknowledgements. The work of CK has been supported by the PECS-98073 contract of the European Space Agency and the Hungarian Space Office, the K-104607 grant of the Hungarian Research Fund (OTKA), the Bolyai Research Fellowship of the Hungarian Academy of Sciences, and the NKFIH grant GINOP-2.3.2-15-2016-00003. EV acknowledges the support of the German DLR project number 50 OR 1108. Part of the funding for GROND (both hardware as well as personnel) was generously granted by the Leibniz-Prize to Prof. G. Hasinger (DFG grant HA 1850/28-1). The work of JĎ was supported by the grant 15-04816S of the Czech Science Foundation. MJK and YJC were partially supported by the National Research Council of Fundamental Science & Technology through a National Agenda Project "Development of Electro-optic Space Surveillance System" and by matching funds from the Korea Astronomy and Space Science Institute. The work of SH was supported by the Hypervelocity Impact Facility, ISAS, JAXA. The work of MI and HY was supported by research programs through the National Research Foundation of Korea (NRF) funded by the Korean government (MEST) (No. 2012R1A4A1028713 and 2015R1D1A1A01060025). PS acknowledges support through the Sofja Kovalevskaja Award from the Alexander von Humboldt Foundation of Germany. The work of MD was performed in the context of the NEOShield-2 project, which has received funding from the European Union's Horizon 2020 research and innovation programme under grant agreement No. 640351. MD was also supported by the project 11-BS56-008 (SHOCKS) of the French Agence Nationale de la Recherche (ANR).

We thank to M. Yoshikawa (ISAS) who offered his continuous advice and encouragement, and B. Gundlach for support in calculating grain sizes. We thank J. Elliott for the GROND test observations on May 27/28, 2012 and S. Larson for providing additional lightcurve observations.

The research leading to these results has received funding from the European Union's Horizon 2020 Research and Innovation Programme, under Grant Agreement no 687378.

Table 3. AKARI-IRC observations of 162173 Ryugu: the colour-corrected flux densities FD at reference wavelengths λ_c , together with the observational error (σ) and the absolute flux error (σ_{abs}).

JD mid-time	r [AU]	Δ [AU]	α [°]	Band λ_c [μm]	FD [mJy]	σ [mJy]	σ_{abs} [mJy]
2454236.53572	1.414394	0.992030	+45.63	L15 15.0	7.61	0.20	0.43
2454236.53718	1.414394	0.992019	+45.63	L24 24.0	7.37	0.25	0.45

Table 4. Subaru-COMICS colour-corrected flux densities FD at reference wavelength λ_c of 162173 Ryugu after our new reduction and calibration scheme (including 5% error for the absolute flux calibration).

JD mid-time	r [AU]	Δ [AU]	α [°]	λ_c [μm]	FD [mJy]	σ [mJy]
2454341.00663	1.28725	0.30667	+22.29	8.8	59	8
2454341.04788	1.28714	0.30654	+22.28	8.8	51	6
2454341.09713	1.28702	0.30639	+22.27	8.8	55	8
2454341.10150	1.28701	0.30637	+22.26	8.8	54	17
2454340.98996	1.28729	0.30673	+22.29	9.7	76	26
2454340.98371	1.28730	0.30675	+22.30	10.5	85	12
2454340.96392	1.28735	0.30681	+22.30	11.7	109	12
2454340.96842	1.28734	0.30680	+22.30	11.7	111	12
2454340.99529	1.28728	0.30671	+22.29	11.7	116	11
2454341.01079	1.28724	0.30666	+22.29	11.7	110	11
2454341.02829	1.28719	0.30660	+22.28	11.7	116	14
2454341.03246	1.28718	0.30659	+22.28	11.7	98	13
2454341.03612	1.28717	0.30658	+22.28	11.7	106	12
2454341.05558	1.28713	0.30652	+22.28	11.7	90	15
2454341.05917	1.28712	0.30651	+22.28	11.7	93	11
2454341.07333	1.28708	0.30646	+22.27	11.7	104	14
2454341.08925	1.28704	0.30641	+22.27	11.7	104	17
2454341.04563	1.28715	0.30655	+22.28	12.4	119	15

Table 5. Spitzer/IRAC "Map PC" $3.6\ \mu\text{m}$ and $4.5\ \mu\text{m}$ observations of 162173 Ryugu as part of the Spitzer Proposal ID #90145. Above: observation start and end times (UTC) of all AORs. The AOR keys & labels are related to observations in the *Spitzer Heritage Archive*. Below: fluxes in the two photometric channels, averaged per epoch. Ephemeris information (r , Δ , α) is given for observation midtime, with positive phase angles α before and negative after opposition. The latter is calculated as the average of the midtimes of the analysed data frames in both channels not corrected for light travel time. The colour-corrected monochromatic flux densities FD at reference wavelengths λ_c ($3.55\ \mu\text{m}$ & $4.49\ \mu\text{m}$) are given. The flux uncertainty includes the $\sim 5\%$ calibration uncertainty. $\langle \text{lc1} \rangle$ and $\langle \text{lc2} \rangle$ are lightcurve-averaged flux densities.

AORKEY	AOR label	Start time	End time	Duration [hms]				
48355840	IRACPC_1999_JU3_lc1a	2013-02-10 20:07:16	2013-02-11 01:03:33	04h56m17s				
48355584	IRACPC_1999_JU3_lc1b	2013-02-11 01:10:47	2013-02-11 04:03:00	02h52m13s				
48355328	IRACPC_1999_JU3_lc2a	2013-05-02 11:47:00	2013-05-02 16:55:06	05h08m06s				
48355072	IRACPC_1999_JU3_lc2b	2013-05-02 17:03:38	2013-05-02 19:52:28	02h48m50s				
47925760	IRACPC_1999_JU3-p1c	2013-01-20 02:01:04	2013-01-20 02:10:37	00h09m33s				
47926016	IRACPC_1999_JU3-p1d	2013-01-27 23:00:59	2013-01-27 23:10:34	00h09m35s				
47926272	IRACPC_1999_JU3-p1e	2013-01-31 01:09:29	2013-01-31 01:19:04	00h09m35s				
47926528	IRACPC_1999_JU3-p1f	2013-02-09 02:24:19	2013-02-09 02:33:58	00h09m39s				
47926784	IRACPC_1999_JU3-p2a	2013-04-28 19:24:40	2013-04-28 19:34:43	00h10m03s				
47927040	IRACPC_1999_JU3-p2b	2013-05-05 02:37:37	2013-05-05 02:47:40	00h10m03s				
47927296	IRACPC_1999_JU3-p2c	2013-05-09 23:41:59	2013-05-09 23:51:58	00h09m59s				
47927552	IRACPC_1999_JU3-p2d	2013-05-15 13:42:43	2013-05-15 13:52:45	00h10m02s				
47927808	IRACPC_1999_JU3-p2e	2013-05-23 21:16:01	2013-05-23 21:26:18	00h10m17s				
47928064	IRACPC_1999_JU3-p2f	2013-05-29 09:45:27	2013-05-29 09:55:53	00h10m26s				
Label	Julian Date mid-time	r [AU]	Δ [AU]	α [$^\circ$]	monochromatic FD and abs. error [mJy]			
$\langle \text{lc1} \rangle$	2456334.50201	1.01214	0.22957	-83.6	FD _{3.55}	err _{3.55}	FD _{4.49}	err _{4.49}
$\langle \text{lc2} \rangle$	2456415.15792	1.00661	0.11129	-85.0	4.65	0.25	26.00	1.40
p1c	2456312.58738	1.06780	0.24935	-71.6	1.21	0.07	7.01	0.39
p1d	2456320.46234	1.04627	0.24442	-76.0	1.12	0.07	6.42	0.35
p1e	2456323.55157	1.03824	0.24181	-77.7	1.19	0.07	6.58	0.36
p1f	2456332.60356	1.01637	0.23202	-82.6	1.33	0.08	7.20	0.40
p2a	2456411.31228	0.99889	0.11258	-88.9	3.94	0.22	22.06	1.20
p2b	2456417.61294	1.01186	0.11093	-82.3	5.38	0.30	29.00	1.57
p2c	2456422.49095	1.02296	0.11138	-76.6	5.01	0.28	28.16	1.52
p2d	2456428.07480	1.03666	0.11392	-69.9	6.42	0.35	35.48	1.92
p2e	2456436.38969	1.05869	0.12205	-60.2	6.95	0.38	35.25	1.91
p2f	2456441.91017	1.07419	0.13051	-54.5	6.10	0.34	30.23	1.63

Table 6. GROND data set of observations 162173 Ryugu. Note, that phase angles α are positive before and negative after opposition.

Julian Date	Y/M/D	H:M:S	obsrunid	seqnum	r[AU]	D[AU]	α [$^{\circ}$]
2456075.58586	2012/5/28	02:03:38.7	1	1	1.35995	0.34822	+4.92
2456075.59086	2012/5/28	02:10:50.2	1	2	1.35996	0.34822	+4.91
2456087.54855	2012/6/9	01:09:54.8	2	1	1.37879	0.36931	-8.60
2456087.55395	2012/6/9	01:17:41.0	2	2	1.37880	0.36932	-8.61
2456087.55891	2012/6/9	01:24:50.0	2	3	1.37880	0.36934	-8.62
2456087.56394	2012/6/9	01:32:04.8	2	4	1.37881	0.36935	-8.62
2456087.56892	2012/6/9	01:39:14.7	2	5	1.37882	0.36936	-8.63
2456087.57394	2012/6/9	01:46:28.6	2	6	1.37882	0.36937	-8.63
2456087.57900	2012/6/9	01:53:45.3	2	7	1.37883	0.36939	-8.64
2456087.58585	2012/6/9	02:03:37.5	3	1	1.37884	0.36941	-8.64
2456087.59087	2012/6/9	02:10:50.8	3	2	1.37885	0.36942	-8.65
2456087.59590	2012/6/9	02:18:05.6	3	3	1.37885	0.36943	-8.66
2456087.60084	2012/6/9	02:25:12.7	3	4	1.37886	0.36945	-8.66
2456087.60582	2012/6/9	02:32:23.2	3	5	1.37887	0.36946	-8.67
2456087.61082	2012/6/9	02:39:34.5	3	6	1.37888	0.36947	-8.67
2456087.61585	2012/6/9	02:46:49.3	3	7	1.37888	0.36949	-8.68
2456087.62087	2012/6/9	02:54:03.1	3	8	1.37889	0.36950	-8.68
2456087.67131	2012/6/9	04:06:40.8	4	1	1.37896	0.36964	-8.74
2456087.67915	2012/6/9	04:17:58.6	4	2	1.37897	0.36966	-8.75
2456087.68411	2012/6/9	04:25:06.7	4	3	1.37898	0.36967	-8.75
2456087.68906	2012/6/9	04:32:14.7	4	4	1.37899	0.36969	-8.76
2456087.69403	2012/6/9	04:39:24.0	4	5	1.37899	0.36970	-8.76
2456087.69899	2012/6/9	04:46:33.1	4	6	1.37900	0.36972	-8.77
2456087.70740	2012/6/9	04:58:39.7	5	1	1.37901	0.36974	-8.78
2456087.71614	2012/6/9	05:11:14.3	6	1	1.37903	0.36977	-8.79
2456087.72124	2012/6/9	05:18:34.9	6	2	1.37903	0.36978	-8.79
2456087.72618	2012/6/9	05:25:42.0	6	3	1.37904	0.36979	-8.80
2456087.73113	2012/6/9	05:32:50.0	6	4	1.37905	0.36981	-8.80
2456087.73609	2012/6/9	05:39:58.4	6	5	1.37905	0.36982	-8.81
2456087.74102	2012/6/9	05:47:04.5	6	6	1.37906	0.36984	-8.82
2456087.75022	2012/6/9	06:00:18.8	7	1	1.37907	0.36986	-8.82
2456087.75519	2012/6/9	06:07:28.8	7	2	1.37908	0.36988	-8.83
2456087.76014	2012/6/9	06:14:36.0	7	3	1.37909	0.36989	-8.84
2456087.76512	2012/6/9	06:21:46.0	7	4	1.37909	0.36991	-8.84
2456087.77008	2012/6/9	06:28:54.5	7	5	1.37910	0.36992	-8.85
2456087.77505	2012/6/9	06:36:04.4	7	6	1.37911	0.36994	-8.85
2456087.78008	2012/6/9	06:43:18.7	7	7	1.37912	0.36995	-8.86
2456087.78509	2012/6/9	06:50:31.9	7	8	1.37912	0.36997	-8.86
2456088.68616	2012/6/10	04:28:04.2	8	1	1.38039	0.37253	-9.81
2456088.69113	2012/6/10	04:35:13.9	8	2	1.38039	0.37255	-9.82
2456088.69613	2012/6/10	04:42:25.6	8	3	1.38040	0.37256	-9.82
2456088.70113	2012/6/10	04:49:37.7	8	4	1.38041	0.37258	-9.83
2456088.70717	2012/6/10	04:58:19.8	9	1	1.38041	0.37260	-9.84
2456088.71345	2012/6/10	05:07:22.1	9	2	1.38042	0.37262	-9.84
2456088.71843	2012/6/10	05:14:32.4	9	3	1.38043	0.37263	-9.85
2456088.72343	2012/6/10	05:21:44.4	9	4	1.38044	0.37265	-9.85
2456088.72831	2012/6/10	05:28:45.8	9	5	1.38044	0.37266	-9.86
2456088.73326	2012/6/10	05:35:53.8	9	6	1.38045	0.37268	-9.87
2456088.73817	2012/6/10	05:42:58.0	9	7	1.38046	0.37269	-9.87
2456088.74315	2012/6/10	05:50:08.1	9	8	1.38046	0.37271	-9.88
2456088.74946	2012/6/10	05:59:13.5	10	1	1.38047	0.37273	-9.88
2456088.75444	2012/6/10	06:06:23.5	10	2	1.38048	0.37274	-9.89
2456088.75932	2012/6/10	06:13:25.6	10	3	1.38049	0.37276	-9.89
2456088.76423	2012/6/10	06:20:29.8	10	4	1.38049	0.37277	-9.90
2456088.76919	2012/6/10	06:27:37.9	10	5	1.38050	0.37279	-9.90
2456088.77419	2012/6/10	06:34:49.9	10	6	1.38051	0.37280	-9.91
2456088.77913	2012/6/10	06:41:56.4	10	7	1.38051	0.37282	-9.91
2456088.78409	2012/6/10	06:49:05.5	10	8	1.38052	0.37283	-9.92
2456088.79049	2012/6/10	06:58:18.0	11	1	1.38053	0.37285	-9.93
2456088.79539	2012/6/10	07:05:21.7	11	2	1.38054	0.37287	-9.93
2456088.80039	2012/6/10	07:12:33.7	11	3	1.38054	0.37288	-9.94
2456088.80530	2012/6/10	07:19:38.2	11	4	1.38055	0.37290	-9.94

References

- Abe, M., Kawakami, K., Hasegawa, S. et al. 2008, COSPAR Scientific Assembly, B04-0061-08
- Balog, Z., Müller, T. G., Nielbock, M. et al. 2014, *Exp. Astronomy*, 37, 129
- Binzel, R. P., Perozzi, E., Rivkin, A. S., Rossi, A., Harris, A. W., Bus, S. J., Valsecchi, G. B., Slivan, S. M. 2004, *Meteorit. Planet. Sci.*, 39, 351
- Bowell, E. 1989, *Asteroids II; Proceedings of the Conference*, Tucson, AZ, Mar. 8-11, 1988 (A90-27001 10-91), University of Arizona Press, 1989, p. 524-556
- Campins, H., Emery, J.P., Kelley, et al. 2009, *A&A* 503, L17-L20
- Cohen, M., Walker, R. G., Carter, B. et al., 1999, *AJ*, 117, 1864
- Đurech, J., Delbo, M., & Carry, B. 2012, *LPI Contributions*, 1667, 6118
- Egusa, F., Usui, F., Murata, K., et al. 2016, *PASJ* 68, 19
- Fazio, G.G., Hora, J.L., Allen, L.E., et al. 2004, *ApJS* 154, 10
- Greiner, J., Bornemann, W., Clemens, C. et al. 2008, *PASP* 120, 405-424
- Gundlach, B. & Blum, J. 2013, *Icarus* 223, 479-492
- Hasegawa, S., Müller, T. G., Kawakami, K., Kasuga, T., Wada, T., Ita, Y., Takato, N., Terada, H., Fujiyoshi, T., Abe, M. 2008, *PASJ* 60, 399
- Hora, J. L., Carey, S., Surace, J. et al. 2008, *PASP*, 120, 1233
- Ishiguro, M., Kuroda, D., Hasegawa, S. et al. 2014, *ApJ* 792, 74
- Kaasalainen, M. & Torppa, J. 2001, *Icarus*, 153, 24
- Kaasalainen, M., Torppa, J. & Muinonen, K. 2001, *Icarus*, 153, 37
- Kaasalainen, M. 2011, *Inverse Problems and Imaging* 5, 37
- Kiss, C., Müller, T. G., Vilnius, E. et al. 2014, *Exp. Astron.*, 37, 161
- Krühler, T., Küpcü, Y. A., Greiner, J. et al. 2008, *ApJ*, 685, 376
- Lagerros, J. S. V. 1996, *A&A* 310, 1011
- Lagerros, J. S. V. 1997, *A&A* 325, 1226
- Lagerros, J. S. V. 1998, *A&A* 332, 1123
- Lazzaro, D., Barucci, M.A., Perna, D. et al. 2013, *A&A* 549, L2
- Moskovitz, N. A., Abe, S. Pan, K.-S. et al. 2013, *Icarus* 224, 24-31
- Müller, T. G. & Lagerros, J. S. V. 1998, *A&A*, 338, 340-352
- Müller, T. G. 2002, *M&PS*, 37, 1919
- Müller, T. G., Sterzik, M. F., Schütz, O. et al. 2004, *A&A*, 424, 1075-1080
- Müller, T. G., Sekiguchi, T., Kaasalainen, M. et al. 2005, *A&A*, 443, 347-355
- Mueller, M., Delbo, M., Hora, J. L., et al. 2011, *AJ* 141, 109
- Müller, T. G., Đurech, J., Hasegawa, S. et al. 2011, *A&A*, 525, 145
- Müller, T. G., O'Rourke, L., Barucci, A. M. et al. 2012, *A&A*, 548, 36-45
- Müller, T. G., Hasegawa, S. & Usui, F. 2014, *PASJ* 66, 52
- Mueller, M., Emery, J., Rivkin, A. et al. 2012, *Spitzer Proposal ID #90145*
- Mueller, M., Emery, J., Rivkin, A. et al. 2013, *American Astronomical Society, DPS meeting #45, #304.01*
- Nolan, M. C., Magri, C., Howell, E. S. et al. 2013, *Icarus*, 226, 629
- Opeil, C.P., Consolmagno, G.J., Britt, D.T. 2010, *Icarus* 208, 449-454
- O'Rourke, L., Müller, T., Valtchanov, I. et al. 2012, *Planetary and Space Science*, 66, 192-199
- O'Rourke, L., Müller, T., Altieri, B. et al. 2014, *Asteroids, Comets, Meteors 2014. Proceedings of the conference held 30 June - 4 July, 2014 in Helsinki, Finland*. Edited by K. Muinonen et al. 2014, p. 400
- Pilbratt, G. L., Riedinger, J. R., Passvogel, T. et al. 2010, *A&A*, 518, L1
- Pinilla-Alonso, N., Lorenzi, V., Campins H. et al. 2013, *A&A* 552, A79
- Poglitsch, A., Waelkens, C., Geis, N. et al. 2010, *A&A*, 518, L2
- Rozitis, B. & Green, S. F. 2011, *MNRAS*, 415, 2042
- Tanabe, T., Sakon, I., Cohen, M. et al. 2008, *PASJ*, 60, 375
- Trilling, D. E., Mueller, M., Hora, J. L., et al. 2010, *AJ*, 140, 770
- Werner, M., Roellig, T., Low, F., et al. 2004, *ApJS* 154, 1
- Yu, L.-L., Ji, J.-H., Wang, S. 2014, *Chinese Astronomy and Astrophysics* 38, 317

Appendix A: Spitzer-IRAC point-and-shoot observations of 162173 (1999 JU₃)

The Spitzer-IRAC point-and-shoot fluxes of Ryugu from Spitzer PID 90145 (PI: M. Mueller) are given in Table A.1. All fluxes given below are absolutely calibrated in-band IRAC fluxes, the solar reflection is not subtracted, and the thermal flux component not colour-corrected. The times given are AOR start time as measured onboard Spitzer (UTC), that is, not corrected for light travel time between asteroid and spacecraft.

Appendix B: Spitzer-IRAC lightcurve observations of 162173 Ryugu

The Spitzer-IRAC lightcurve fluxes of Ryugu from Spitzer PID 90145 (PI: M. Mueller) are given in Tables B.1, B.2, B.3, and B.4. All fluxes given below are absolutely calibrated in-band IRAC fluxes, the solar reflection is not subtracted and the thermal flux component is not colour corrected. The times given are AOR start time as measured onboard Spitzer (UTC), that is, not corrected for light travel time between asteroid and spacecraft.

Appendix C: Ground-based observations of 162173 Ryugu with GROND

The GROND data are explained in Section 3. The reduced and calibrated data are presented in Tables C.1 and C.2.

Table A.1. Spitzer-IRAC point-and-shoot observation of 162173 Ryugu from January to May 2013.

Label	DATE_OBS	Channel 1			Flux [μ Jy]	Flux _{err} [μ Jy]	Channel 2			Flux [μ Jy]	Flux _{err} [μ Jy]
		mag	mag _{err}	S/N			mag	mag _{err}	S/N		
1999_JU3c	2013-01-20T02:05:04	13.32	0.03	38	1318.7	34.3	10.978	0.011	91	7300.4	80.3
1999_JU3d	2013-01-27T23:05:00	13.41	0.03	37	1218.3	32.9	11.074	0.011	91	6682.6	73.5
1999_JU3e	2013-01-31T01:13:30	13.34	0.03	38	1293.5	33.6	11.046	0.011	91	6857.2	75.4
1999_JU3f	2013-02-09T02:28:22	13.22	0.03	40	1442.0	36.0	10.948	0.011	91	7505.0	82.6
1999_JU3-p2a	2013-04-28T19:26:46	12.04	0.01	71	4287.0	60.0	9.73	0.01	167	22979.9	137.9
1999_JU3-p2b	2013-05-05T02:39:45	11.70	0.01	83	5847.3	70.2	9.44	0.01	200	30209.8	151.0
1999_JU3-p2c	2013-05-09T23:44:05	11.78	0.01	77	5446.9	70.8	9.47	0.01	200	29332.4	146.7
1999_JU3-p2d	2013-05-15T13:44:49	11.51	0.01	91	6978.3	76.8	9.22	0.01	200	36961.4	184.8
1999_JU3-p2e	2013-05-23T21:18:11	11.43	0.01	91	7553.6	83.1	9.22	0.01	200	36723.8	183.6
1999_JU3-p2f	2013-05-29T09:47:38	11.57	0.01	91	6627.5	72.9	9.39	0.01	200	31488.2	157.4

Table B.1. Spitzer-IRAC lightcurve observation of 162173 Ryugu from 10/11th February, 2013, channel 1. The estimated flux uncertainty is 18 μ Jy.

DATE_OBS	MJD_OBS	Flux [μ Jy]	DATE_OBS	MJD_OBS	Flux [μ Jy]
2013-02-10T20:11:48.655	56333.84154	1394.5	2013-02-10T23:57:08.084	56333.99801	1495.0
2013-02-10T20:18:44.643	56333.84635	1374.6	2013-02-11T00:04:06.072	56334.00285	1503.1
2013-02-10T20:25:40.639	56333.85116	1392.2	2013-02-11T00:11:02.466	56334.00767	1498.2
2013-02-10T20:32:39.041	56333.85601	1411.2	2013-02-11T00:17:59.266	56334.01249	1539.9
2013-02-10T20:41:34.231	56333.86220	1399.5	2013-02-11T00:24:18.067	56334.01688	1506.3
2013-02-10T20:48:51.430	56333.86726	1385.0	2013-02-11T00:31:14.461	56334.02170	1487.6
2013-02-10T20:55:47.019	56333.87207	1407.6	2013-02-11T00:38:11.651	56334.02652	1492.7
2013-02-10T21:02:45.816	56333.87692	1430.3	2013-02-11T00:45:08.452	56334.03135	1526.2
2013-02-10T21:09:42.214	56333.88174	1418.7	2013-02-11T00:52:04.029	56334.03616	1449.2
2013-02-10T21:16:39.002	56333.88656	1438.5	2013-02-11T01:15:35.614	56334.05250	1398.2
2013-02-10T21:22:55.396	56333.89092	1478.4	2013-02-11T01:22:57.215	56334.05761	1337.4
2013-02-10T21:29:52.997	56333.89575	1437.0	2013-02-11T01:30:17.605	56334.06270	1371.7
2013-02-10T21:36:50.180	56333.90058	1433.1	2013-02-11T01:37:39.991	56334.06782	1306.8
2013-02-10T21:43:46.988	56333.90541	1396.0	2013-02-11T01:45:01.596	56334.07294	1309.3
2013-02-10T21:50:42.570	56333.91021	1359.5	2013-02-11T01:52:46.181	56334.07831	1360.8
2013-02-10T21:57:59.769	56333.91528	1345.3	2013-02-11T02:00:08.981	56334.08344	1335.0
2013-02-10T22:04:59.370	56333.92013	1370.6	2013-02-11T02:07:29.778	56334.08854	1364.3
2013-02-10T22:12:54.162	56333.92563	1355.6	2013-02-11T02:15:56.176	56334.09440	1390.8
2013-02-10T22:19:50.962	56333.93045	1359.5	2013-02-11T02:24:20.573	56334.10024	1409.3
2013-02-10T22:26:46.548	56333.93526	1348.6	2013-02-11T02:31:01.171	56334.10487	1431.5
2013-02-10T22:33:06.946	56333.93966	1349.2	2013-02-11T02:39:27.158	56334.11073	1441.4
2013-02-10T22:40:02.934	56333.94448	1315.2	2013-02-11T02:46:49.146	56334.11585	1468.5
2013-02-10T22:46:59.730	56333.94930	1348.4	2013-02-11T02:54:11.950	56334.12097	1453.8
2013-02-10T22:53:54.925	56333.95411	1336.6	2013-02-11T03:01:31.938	56334.12606	1420.7
2013-02-10T23:01:52.116	56333.95963	1372.0	2013-02-11T03:09:16.527	56334.13144	1420.5
2013-02-10T23:08:11.318	56333.96402	1365.3	2013-02-11T03:17:43.323	56334.13731	1396.7
2013-02-10T23:15:08.111	56333.96884	1375.9	2013-02-11T03:25:04.120	56334.14241	1436.7
2013-02-10T23:22:04.907	56333.97367	1404.1	2013-02-11T03:32:26.920	56334.14753	1407.6
2013-02-10T23:28:59.301	56333.97846	1391.8	2013-02-11T03:39:48.509	56334.15264	1415.8
2013-02-10T23:35:59.297	56333.98333	1402.8	2013-02-11T03:46:29.899	56334.15729	1427.5
2013-02-10T23:42:55.284	56333.98814	1465.4	2013-02-11T03:53:53.899	56334.16243	1397.2
2013-02-10T23:50:12.885	56333.99320	1429.0	2013-02-11T04:01:14.683	56334.16753	1408.5

Table B.2. Spitzer-IRAC lightcurve observation of 162173 Ryugu from 10/11th February, 2013, channel 2. The estimated flux uncertainty is 41 μ Jy.

DATE_OBS	MJD_OBS	Flux [μ Jy]	DATE_OBS	MJD_OBS	Flux [μ Jy]
2013-02-10T20:14:16.651	56333.84325	7498.1	2013-02-11T00:03:36.873	56334.00251	7938.7
2013-02-10T20:22:13.041	56333.84876	7408.8	2013-02-11T00:11:33.271	56334.00802	8012.1
2013-02-10T20:30:09.439	56333.85428	7491.1	2013-02-11T00:21:48.067	56334.01514	7982.7
2013-02-10T20:39:04.630	56333.86047	7436.1	2013-02-11T00:30:44.855	56334.02135	7990.0
2013-02-10T20:48:21.825	56333.86692	7491.1	2013-02-11T00:40:39.655	56334.02824	8019.5
2013-02-10T20:56:17.426	56333.87242	7567.4	2013-02-11T00:50:34.842	56334.03513	7975.3
2013-02-10T21:07:13.015	56333.88001	7715.2	2013-02-11T01:16:07.016	56334.05286	7456.7
2013-02-10T21:15:08.600	56333.88552	7651.5	2013-02-11T01:24:31.007	56334.05869	7273.6
2013-02-10T21:24:25.798	56333.89197	7779.4	2013-02-11T01:33:58.206	56334.06526	7180.4
2013-02-10T21:34:21.790	56333.89886	7665.6	2013-02-11T01:42:24.990	56334.07112	7147.4
2013-02-10T21:41:17.387	56333.90367	7525.7	2013-02-11T01:50:09.990	56334.07650	7334.1
2013-02-10T21:49:14.976	56333.90920	7408.8	2013-02-11T01:57:30.782	56334.08161	7206.9
2013-02-10T21:58:29.765	56333.91562	7340.9	2013-02-11T02:09:05.176	56334.08964	7320.6
2013-02-10T22:06:28.159	56333.92116	7200.3	2013-02-11T02:16:27.164	56334.09476	7402.0
2013-02-10T22:16:21.760	56333.92803	7193.6	2013-02-11T02:25:55.558	56334.10134	7602.4
2013-02-10T22:23:19.747	56333.93287	7088.4	2013-02-11T02:33:40.553	56334.10672	7679.8
2013-02-10T22:33:35.743	56333.94000	7167.2	2013-02-11T02:44:12.552	56334.11403	7616.4
2013-02-10T22:41:32.547	56333.94552	7094.9	2013-02-11T02:51:34.149	56334.11915	7750.8
2013-02-10T22:49:27.331	56333.95101	7134.2	2013-02-11T03:01:00.938	56334.12571	7736.6
2013-02-10T22:57:24.132	56333.95653	7167.2	2013-02-11T03:09:50.734	56334.13184	7616.4
2013-02-10T23:05:21.318	56333.96205	7134.2	2013-02-11T03:19:17.526	56334.13840	7553.5
2013-02-10T23:13:39.720	56333.96782	7240.2	2013-02-11T03:27:41.514	56334.14423	7456.7
2013-02-10T23:22:34.110	56333.97401	7402.0	2013-02-11T03:35:05.119	56334.14936	7463.6
2013-02-10T23:29:29.692	56333.97882	7539.6	2013-02-11T03:44:56.903	56334.15621	7532.7
2013-02-10T23:37:28.093	56333.98435	7665.6	2013-02-11T03:54:24.903	56334.16279	7546.5
2013-02-10T23:45:44.081	56333.99009	7679.8	2013-02-11T04:02:48.488	56334.16862	7487.7
2013-02-10T23:53:41.291	56333.99562	7808.1			

Table B.3. Spitzer-IRAC lightcurve observation of 162173 Ryugu from 2nd May, 2013, channel 1. The estimated flux uncertainty is $49\ \mu\text{Jy}$.

DATE_OBS	MJD_OBS	Flux [μJy]	DATE_OBS	MJD_OBS	Flux [μJy]
2013-05-02T11:48:43.708	56414.49217	5148.0	2013-05-02T15:50:18.343	56414.65993	4534.4
2013-05-02T11:52:43.704	56414.49495	4992.9	2013-05-02T15:54:17.542	56414.66270	4407.4
2013-05-02T11:55:56.512	56414.49718	5049.7	2013-05-02T15:57:31.131	56414.66494	4549.1
2013-05-02T11:59:56.508	56414.49996	5009.1	2013-05-02T16:01:32.330	56414.66774	4511.6
2013-05-02T12:03:10.504	56414.50220	5015.3	2013-05-02T16:04:44.729	56414.66996	4539.4
2013-05-02T12:07:12.504	56414.50501	5134.1	2013-05-02T16:08:45.525	56414.67275	4428.4
2013-05-02T12:10:23.699	56414.50722	4985.1	2013-05-02T16:11:19.119	56414.67453	4688.8
2013-05-02T12:14:24.495	56414.51001	5104.7	2013-05-02T16:15:19.126	56414.67730	4566.4
2013-05-02T12:18:32.089	56414.51287	5069.8	2013-05-02T16:18:32.317	56414.67954	4565.8
2013-05-02T12:22:39.690	56414.51574	4989.2	2013-05-02T16:22:31.516	56414.68231	4604.6
2013-05-02T12:25:13.682	56414.51752	5203.0	2013-05-02T16:25:45.106	56414.68455	4681.8
2013-05-02T12:29:14.084	56414.52030	5088.8	2013-05-02T16:29:45.512	56414.68733	4706.6
2013-05-02T12:32:26.084	56414.52252	4967.6	2013-05-02T16:32:57.109	56414.68955	4520.7
2013-05-02T12:36:27.674	56414.52532	5027.8	2013-05-02T16:36:59.113	56414.69235	4604.1
2013-05-02T12:39:41.275	56414.52756	5116.3	2013-05-02T16:40:11.503	56414.69458	4767.7
2013-05-02T12:43:40.075	56414.53032	5090.1	2013-05-02T16:44:12.296	56414.69736	4529.5
2013-05-02T12:46:52.466	56414.53255	5086.9	2013-05-02T16:47:24.300	56414.69959	4640.6
2013-05-02T12:50:53.669	56414.53534	5256.6	2013-05-02T16:50:51.889	56414.70199	4439.5
2013-05-02T12:53:41.661	56414.53759	5188.3	2013-05-02T16:54:52.698	56414.70478	4722.7
2013-05-02T12:58:06.070	56414.54035	5083.9	2013-05-02T17:05:21.681	56414.71206	4644.1
2013-05-02T13:01:20.058	56414.54259	5396.6	2013-05-02T17:09:20.880	56414.71483	4652.0
2013-05-02T13:05:42.453	56414.54563	5236.3	2013-05-02T17:12:34.079	56414.71706	4628.0
2013-05-02T13:08:56.445	56414.54788	5375.9	2013-05-02T17:16:33.274	56414.71983	4679.8
2013-05-02T13:12:56.452	56414.55065	5504.7	2013-05-02T17:19:47.668	56414.72208	4755.1
2013-05-02T13:16:08.854	56414.55288	5258.0	2013-05-02T17:23:48.074	56414.72486	4759.9
2013-05-02T13:20:09.655	56414.55567	5404.2	2013-05-02T17:26:59.664	56414.72708	4797.6
2013-05-02T13:23:22.838	56414.55790	5549.7	2013-05-02T17:31:00.066	56414.72986	4748.1
2013-05-02T13:27:22.451	56414.56068	5472.2	2013-05-02T17:34:14.066	56414.73211	4822.0
2013-05-02T13:30:35.642	56414.56291	5343.2	2013-05-02T17:38:15.257	56414.73490	4913.4
2013-05-02T13:34:34.833	56414.56568	5507.5	2013-05-02T17:41:27.655	56414.73713	4914.3
2013-05-02T13:38:44.439	56414.56857	5600.2	2013-05-02T17:44:54.448	56414.73952	4885.0
2013-05-02T13:41:18.032	56414.57035	5801.8	2013-05-02T17:48:55.256	56414.74231	5008.9
2013-05-02T13:45:17.637	56414.57312	5548.8	2013-05-02T17:52:08.451	56414.74454	4954.5
2013-05-02T13:48:30.821	56414.57536	5631.8	2013-05-02T17:56:09.248	56414.74733	5093.9
2013-05-02T13:52:30.031	56414.57813	5506.6	2013-05-02T17:59:21.236	56414.74955	4922.1
2013-05-02T13:55:44.015	56414.58037	5735.9	2013-05-02T18:03:21.646	56414.75233	4931.0
2013-05-02T13:59:44.812	56414.58316	5716.3	2013-05-02T18:06:34.837	56414.75457	5091.7
2013-05-02T14:02:56.015	56414.58537	5568.5	2013-05-02T18:10:36.044	56414.75736	4952.8
2013-05-02T14:06:57.616	56414.58817	5709.6	2013-05-02T18:13:47.231	56414.75957	5125.6
2013-05-02T14:10:10.815	56414.59040	5749.7	2013-05-02T18:17:48.828	56414.76237	5144.2
2013-05-02T14:14:11.202	56414.59319	5591.1	2013-05-02T18:20:22.035	56414.76414	5212.9
2013-05-02T14:17:23.209	56414.59541	5585.7	2013-05-02T18:24:21.632	56414.76692	5180.0
2013-05-02T14:20:43.607	56414.59773	5453.1	2013-05-02T18:27:34.425	56414.76915	5135.8
2013-05-02T14:23:57.595	56414.59997	5631.5	2013-05-02T18:31:33.624	56414.77192	5226.4
2013-05-02T14:27:57.201	56414.60275	5452.7	2013-05-02T18:34:48.819	56414.77418	5102.8
2013-05-02T14:31:09.204	56414.60497	5388.4	2013-05-02T18:38:49.217	56414.77696	5174.1
2013-05-02T14:35:10.395	56414.60776	5438.7	2013-05-02T18:42:00.416	56414.77917	5284.0
2013-05-02T14:39:17.192	56414.61062	5309.8	2013-05-02T18:46:01.209	56414.78196	5114.8
2013-05-02T14:42:31.188	56414.61286	5339.8	2013-05-02T18:49:14.408	56414.78419	5189.6
2013-05-02T14:46:31.980	56414.61565	5107.4	2013-05-02T18:53:15.212	56414.78698	5187.1
2013-05-02T14:49:43.175	56414.61786	5222.6	2013-05-02T18:56:27.200	56414.78920	5204.9
2013-05-02T14:53:44.382	56414.62065	5161.8	2013-05-02T18:59:54.806	56414.79161	5053.2
2013-05-02T14:57:11.577	56414.62305	5175.6	2013-05-02T19:03:56.403	56414.79440	5167.3
2013-05-02T15:00:25.171	56414.62529	5047.9	2013-05-02T19:07:09.192	56414.79663	5100.9
2013-05-02T15:04:26.374	56414.62808	4862.1	2013-05-02T19:11:10.000	56414.79942	4921.1
2013-05-02T15:07:38.366	56414.63031	5031.6	2013-05-02T19:14:22.387	56414.80165	5025.2
2013-05-02T15:11:39.561	56414.63310	4956.4	2013-05-02T19:18:21.191	56414.80441	5198.8
2013-05-02T15:14:52.760	56414.63533	4793.7	2013-05-02T19:21:35.175	56414.80666	5002.6
2013-05-02T15:18:52.755	56414.63811	4865.5	2013-05-02T19:25:35.983	56414.80944	5065.2
2013-05-02T15:22:05.161	56414.64034	4835.9	2013-05-02T19:28:47.175	56414.81166	5073.1
2013-05-02T15:26:05.157	56414.64312	4637.7	2013-05-02T19:32:49.577	56414.81446	5106.5
2013-05-02T15:29:18.755	56414.64536	4713.8	2013-05-02T19:35:22.780	56414.81624	5101.3
2013-05-02T15:32:38.754	56414.64767	4713.3	2013-05-02T19:39:22.771	56414.81901	5126.8
2013-05-02T15:35:51.946	56414.64991	4574.8	2013-05-02T19:42:35.572	56414.82124	5051.4
2013-05-02T15:39:52.746	56414.65269	4486.3	2013-05-02T19:46:41.962	56414.82410	5201.0
2013-05-02T15:43:05.543	56414.65493	4670.2	2013-05-02T19:50:43.556	56414.82689	5070.2
2013-05-02T15:47:06.343	56414.65771	4565.6			

Table B.4. Spitzer-IRAC lightcurve observation of 162173 Ryugu from 2nd May, 2013, channel 2. The estimated flux uncertainty is $115 \mu\text{Jy}$.

DATE_OBS	MJD_OBS	Flux [μJy]	DATE_OBS	MJD_OBS	Flux [μJy]
2013-05-02T11:48:13.708	56414.49183	26751.5	2013-05-02T15:44:37.945	56414.65599	24874.1
2013-05-02T11:53:15.708	56414.49532	27073.7	2013-05-02T15:48:39.144	56414.65879	24668.8
2013-05-02T11:56:28.509	56414.49755	26875.0	2013-05-02T15:52:45.933	56414.66164	24714.3
2013-05-02T12:02:32.102	56414.50176	27248.8	2013-05-02T15:55:59.530	56414.66388	24578.1
2013-05-02T12:05:44.496	56414.50399	27198.7	2013-05-02T15:59:58.330	56414.66665	24691.5
2013-05-02T12:09:45.691	56414.50678	26999.0	2013-05-02T16:04:13.119	56414.66960	24555.5
2013-05-02T12:13:51.289	56414.50964	27048.8	2013-05-02T16:08:22.721	56414.67249	24646.1
2013-05-02T12:18:09.288	56414.51261	26949.3	2013-05-02T16:12:51.513	56414.67560	24851.2
2013-05-02T12:22:16.089	56414.51546	27123.7	2013-05-02T16:16:51.919	56414.67838	24897.1
2013-05-02T12:26:38.483	56414.51850	27023.9	2013-05-02T16:20:05.517	56414.68062	24714.3
2013-05-02T12:29:51.682	56414.52074	27173.7	2013-05-02T16:24:05.520	56414.68340	24646.1
2013-05-02T12:33:52.088	56414.52352	27148.6	2013-05-02T16:28:19.110	56414.68633	24851.2
2013-05-02T12:37:05.271	56414.52576	27198.7	2013-05-02T16:32:26.715	56414.68920	25058.1
2013-05-02T12:43:08.872	56414.52996	26899.7	2013-05-02T16:38:32.707	56414.69343	24966.0
2013-05-02T12:46:22.071	56414.53220	27349.4	2013-05-02T16:41:43.902	56414.69565	25012.0
2013-05-02T12:51:24.067	56414.53570	27475.7	2013-05-02T16:45:45.097	56414.69844	24759.8
2013-05-02T12:55:39.657	56414.53865	27935.0	2013-05-02T16:49:19.089	56414.70092	24874.1
2013-05-02T12:59:39.656	56414.54143	28245.4	2013-05-02T16:53:20.694	56414.70371	24851.2
2013-05-02T13:03:16.054	56414.54394	28454.3	2013-05-02T17:04:51.283	56414.71170	24782.7
2013-05-02T13:08:26.050	56414.54752	28454.3	2013-05-02T17:08:50.079	56414.71447	25150.6
2013-05-02T13:12:25.644	56414.55030	28612.0	2013-05-02T17:12:02.876	56414.71670	25058.1
2013-05-02T13:15:38.050	56414.55252	28744.1	2013-05-02T17:17:04.473	56414.72019	25547.5
2013-05-02T13:19:38.444	56414.55531	28850.2	2013-05-02T17:22:14.078	56414.72377	25712.7
2013-05-02T13:23:52.842	56414.55825	28876.7	2013-05-02T17:27:32.074	56414.72745	25760.1
2013-05-02T13:27:54.439	56414.56105	29224.6	2013-05-02T17:33:43.663	56414.73176	26094.5
2013-05-02T13:31:07.236	56414.56328	28770.5	2013-05-02T17:38:45.663	56414.73525	26263.2
2013-05-02T13:35:13.634	56414.56613	29522.2	2013-05-02T17:43:22.456	56414.73845	26287.4
2013-05-02T13:39:22.024	56414.56900	29224.6	2013-05-02T17:47:23.248	56414.74124	26408.8
2013-05-02T13:43:46.028	56414.57206	29767.9	2013-05-02T17:50:36.045	56414.74347	26506.2
2013-05-02T13:46:57.629	56414.57428	29795.3	2013-05-02T17:56:39.642	56414.74768	26924.5
2013-05-02T13:50:58.418	56414.57707	29877.8	2013-05-02T18:00:54.439	56414.75063	27123.7
2013-05-02T13:54:11.226	56414.57930	29713.1	2013-05-02T18:06:59.235	56414.75485	27123.7
2013-05-02T13:59:20.816	56414.58288	29932.8	2013-05-02T18:10:12.036	56414.75708	27173.7
2013-05-02T14:03:29.214	56414.58575	29603.8	2013-05-02T18:15:13.637	56414.76057	27551.7
2013-05-02T14:09:40.007	56414.59005	29740.5	2013-05-02T18:19:44.027	56414.76370	27602.5
2013-05-02T14:13:40.014	56414.59282	29822.8	2013-05-02T18:23:50.828	56414.76656	27425.1
2013-05-02T14:16:51.998	56414.59505	29631.1	2013-05-02T18:29:07.620	56414.77023	27577.1
2013-05-02T14:22:16.803	56414.59881	29413.6	2013-05-02T18:34:10.417	56414.77373	27755.4
2013-05-02T14:25:29.591	56414.60104	29224.6	2013-05-02T18:38:18.018	56414.77660	27501.0
2013-05-02T14:29:29.197	56414.60381	29143.9	2013-05-02T18:42:33.217	56414.77955	27678.8
2013-05-02T14:34:46.001	56414.60748	28850.2	2013-05-02T18:46:32.010	56414.78231	27501.0
2013-05-02T14:39:48.391	56414.61098	28428.1	2013-05-02T18:50:46.400	56414.78526	27450.4
2013-05-02T14:43:55.985	56414.61384	28480.5	2013-05-02T18:54:55.599	56414.78814	27223.8
2013-05-02T14:47:09.984	56414.61609	27960.7	2013-05-02T19:00:19.997	56414.79190	27577.1
2013-05-02T14:51:17.179	56414.61895	27935.0	2013-05-02T19:03:32.399	56414.79413	27148.6
2013-05-02T14:55:40.382	56414.62200	27678.8	2013-05-02T19:08:33.996	56414.79762	27374.6
2013-05-02T14:58:53.573	56414.62423	27349.4	2013-05-02T19:13:51.187	56414.80129	27023.9
2013-05-02T15:03:54.772	56414.62772	27023.9	2013-05-02T19:17:50.789	56414.80406	27274.0
2013-05-02T15:08:02.772	56414.63059	27073.7	2013-05-02T19:21:04.378	56414.80630	26974.2
2013-05-02T15:11:16.760	56414.63283	26628.6	2013-05-02T19:27:08.374	56414.81051	26974.2
2013-05-02T15:16:16.767	56414.63631	26579.6	2013-05-02T19:30:21.178	56414.81275	27173.7
2013-05-02T15:20:33.162	56414.63927	25783.9	2013-05-02T19:34:52.373	56414.81588	26875.0
2013-05-02T15:26:35.954	56414.64347	25831.4	2013-05-02T19:38:51.978	56414.81866	27475.7
2013-05-02T15:30:43.950	56414.64634	25453.5	2013-05-02T19:42:04.369	56414.82088	27248.8
2013-05-02T15:35:21.153	56414.64955	25220.2	2013-05-02T19:47:05.962	56414.82437	27526.3
2013-05-02T15:41:26.347	56414.65378	25127.4	2013-05-02T19:50:20.353	56414.82662	27602.5

Table C.1. GROND r' magnitudes and errors of 162173 Ryugu. The zero time in the table corresponds to MJD 56087.04942 (2012-Jun-09 01:11:10 UT in the observer's reference frame) which is the mid time of the first GROND pointing (OB2_1, TDP1). The observation identifiers are OB2_1 ... OB2_7, OB3_1 ... OB3_5, OB4_1 ... OB4_6, OB5_1, OB6_1 ... OB6_7, OB7_1 ... OB7_8, with TDP1, TDP2, TDP3, and TDP4 in each observation. There are approximately 2 h lost (at approximately half time) due to bad weather.

TDT mid time [s]	r' [mag]	r' err [mag]	TDT mid time [s]	r' [mag]	r' err [mag]	TDT mid time [s]	r' [mag]	r' err [mag]
0.00	18.202	0.016	4587.84	18.238	0.023	16269.12	18.230	0.013
103.68	18.178	0.015	4691.52	18.235	0.017	16372.80	18.228	0.018
207.36	18.236	0.019	4795.20	18.230	0.020	16476.48	18.235	0.017
311.04	18.186	0.017	4907.52	18.196	0.018	16588.80	18.214	0.016
423.36	18.195	0.019	5019.84	18.236	0.020	16701.12	18.239	0.018
527.04	18.169	0.029	5123.52	18.203	0.018	16804.80	18.236	0.021
639.36	18.145	0.039	5227.20	18.235	0.023	16908.48	18.186	0.018
743.04	18.205	0.033	5348.16	18.239	0.025	17383.68	18.203	0.021
864.00	18.237	0.026	5451.84	18.223	0.021	17487.36	18.214	0.016
967.68	18.206	0.033	5555.52	18.232	0.034	17591.04	18.179	0.017
1071.36	18.179	0.021	5659.20	18.228	0.018	17703.36	18.210	0.015
1175.04	18.225	0.015	5780.16	18.270	0.035	17815.68	18.230	0.016
1296.00	18.197	0.019	5883.84	18.213	0.051	17919.36	18.250	0.016
1399.68	18.195	0.022	5987.52	18.237	0.038	18023.04	18.223	0.018
1503.36	18.209	0.017	6099.84	18.215	0.035	18126.72	18.231	0.016
1607.04	18.181	0.018	6212.16	18.239	0.057	18247.68	18.254	0.014
1728.00	18.200	0.027	6315.84	18.174	0.041	18351.36	18.244	0.017
1831.68	18.173	0.042	6419.52	18.200	0.029	18455.04	18.251	0.017
1935.36	18.218	0.055	6531.84	18.241	0.022	18558.72	18.262	0.019
2039.04	18.178	0.060	—	—	—	18679.68	18.256	0.016
2160.00	18.261	0.055	13564.80	18.195	0.019	18774.72	18.257	0.023
2263.68	18.153	0.033	13668.48	18.195	0.019	18878.40	18.290	0.020
2367.36	18.209	0.021	13772.16	18.208	0.018	18990.72	18.221	0.018
2471.04	18.198	0.019	13875.84	18.195	0.015	19103.04	18.226	0.016
2592.00	18.229	0.016	14454.72	18.229	0.025	19206.72	18.221	0.016
2704.32	18.192	0.015	14558.40	18.208	0.029	19310.40	18.239	0.017
2808.00	18.209	0.017	14662.08	18.190	0.023	19414.08	18.240	0.017
2911.68	18.208	0.016	14765.76	18.204	0.014	19535.04	18.235	0.016
3188.16	18.228	0.022	14878.08	18.231	0.017	19638.72	18.254	0.020
3291.84	18.195	0.020	14981.76	18.189	0.016	19742.40	18.245	0.017
3395.52	18.213	0.016	15085.44	18.234	0.017	19854.72	18.241	0.017
3499.20	18.184	0.021	15197.76	18.224	0.016	19967.04	18.250	0.017
3620.16	18.248	0.017	15310.08	18.200	0.017	20070.72	18.225	0.017
3723.84	18.215	0.022	15413.76	18.172	0.022	20174.40	18.201	0.018
3827.52	18.242	0.016	15517.44	18.239	0.018	20286.72	18.264	0.017
3939.84	18.220	0.023	15629.76	18.204	0.017	20399.04	18.264	0.019
4052.16	18.231	0.022	15742.08	18.224	0.018	20502.72	18.230	0.020
4155.84	18.185	0.021	15845.76	18.199	0.016	20606.40	18.204	0.017
4259.52	18.218	0.023	15949.44	18.246	0.017	20710.08	18.265	0.018
4363.20	18.215	0.022	16053.12	18.231	0.017			
4475.52	18.208	0.020	16165.44	18.207	0.018			

Table C.2. GROND g' , r' , i' magnitudes and errors of 162173 Ryugu. The zero time in the table corresponds to MJD 56088.18661 (2012-Jun-10 04:28:43 UT in the observer's reference frame) which is the mid time of the first GROND pointing (OB8_1, TDP1). The observation identifiers are OB8_1 ... OB8_4, OB9_1 ... OB9_8, OB10_1 ... OB10_8, OB11_1 ... OB11_4, with TDP1, TDP2, TDP3, and TDP4 in each observation. Note, that one i' measurement is missing due to technical problems.

TDT mid time [s]	g' [mag]	g' err [mag]	r' [mag]	r' err [mag]	i' [mag]	i' err [mag]	TDT mid time [s]	g' [mag]	g' err [mag]	r' [mag]	r' err [mag]	i' [mag]	i' err [mag]
0.00	18.687	0.014	18.232	0.009	18.179	0.015	5468.17	18.719	0.018	18.289	0.015	18.234	0.019
103.68	18.685	0.013	18.211	0.011	18.170	0.015	5572.89	18.703	0.017	18.256	0.015	18.204	0.017
205.72	18.699	0.014	18.234	0.012	18.192	0.015	5677.43	18.715	0.018	18.279	0.015	18.250	0.020
311.64	18.679	0.014	18.238	0.011	18.185	0.015	5782.84	18.701	0.019	18.251	0.015	18.182	0.020
430.53	18.698	0.012	18.251	0.011	18.146	0.015	5893.00	18.684	0.016	18.239	0.015	18.154	0.020
535.16	18.691	0.015	18.255	0.012	18.190	0.015	5996.76	18.694	0.018	18.253	0.015	18.214	0.022
638.58	18.692	0.014	18.226	0.011	18.211	0.015	6099.75	18.716	0.022	18.272	0.015	18.198	0.025
744.77	18.697	0.014	18.230	0.011	18.171	0.015	6204.82	18.660	0.017	18.240	0.015	18.243	0.027
862.01	18.726	0.014	18.235	0.011	18.179	0.015	6314.98	18.707	0.019	18.212	0.018	18.213	0.026
966.56	18.715	0.015	18.243	0.011	18.205	0.012	6420.73	18.689	0.024	18.206	0.017	18.178	0.020
1070.58	18.703	0.014	18.235	0.011	18.204	0.015	6524.67	18.729	0.024	18.223	0.019	18.157	0.025
1178.76	18.720	0.014	18.269	0.011	18.227	0.014	6630.68	18.692	0.022	18.233	0.019	18.193	0.025
1296.17	18.685	0.015	18.245	0.011	18.189	0.016	6746.03	18.682	0.022	18.228	0.019	18.229	0.018
1400.54	18.693	0.014	18.264	0.012	18.194	0.015	6847.63	18.670	0.024	18.225	0.019	18.171	0.025
1506.82	18.719	0.015	18.239	0.012	18.214	0.016	6952.78	18.672	0.025	18.227	0.019	18.152	0.026
1612.66	18.730	0.015	18.257	0.012	18.227	0.013	7058.62	18.712	0.027	18.229	0.022	18.171	0.028
1923.70	18.717	0.016	18.287	0.013	18.218	0.014	7176.04	18.702	0.024	18.291	0.022	18.132	0.028
2029.19	18.744	0.016	18.262	0.012	18.228	0.015	7277.64	18.670	0.028	18.230	0.025	18.162	0.031
2134.86	18.730	0.016	18.280	0.012	18.238	0.018	7382.71	18.670	0.030	18.206	0.025	18.115	0.030
2240.61	18.752	0.018	18.285	0.012	18.192	0.018	7488.81	18.677	0.032	18.231	0.025	18.208	0.028
2354.92	18.724	0.016	18.270	0.013	18.219	0.018	7600.78	18.717	0.032	18.167	0.031	18.245	0.047
2460.41	18.704	0.013	18.287	0.013	18.217	0.014	7704.72	18.647	0.037	18.262	0.033	18.173	0.042
2564.70	18.726	0.018	18.278	0.013	18.197	0.018	7808.66	18.673	0.037	18.209	0.033	18.204	0.042
2670.62	18.729	0.017	18.275	0.013	18.167	0.018	7914.59	18.698	0.034	18.210	0.033	18.162	0.043
2789.16	18.724	0.017	18.263	0.013	18.237	0.019	8033.13	18.648	0.045	18.189	0.034	18.107	0.047
2891.55	18.715	0.018	18.310	0.014	18.237	0.019	8136.72	18.663	0.040	18.204	0.028	18.135	0.045
2996.61	18.730	0.017	18.281	0.014	18.245	0.018	8238.84	18.656	0.041	18.231	0.033	18.157	0.046
3102.62	18.739	0.015	18.279	0.014	18.210	0.019	8344.43	18.576	0.033	18.169	0.027	18.033	0.034
3217.02	18.715	0.015	18.271	0.014	18.191	0.019	8455.97	18.626	0.032	18.196	0.027	18.113	0.034
3318.71	18.723	0.016	18.277	0.014	18.241	0.022	8558.70	18.710	0.036	18.267	0.028	18.224	0.037
3420.84	18.720	0.018	18.297	0.014	18.205	0.021	8660.65	18.617	0.036	18.247	0.033	18.216	0.040
3525.72	18.720	0.018	18.296	0.014	18.229	0.020	8765.71	18.669	0.043	18.195	0.033	18.198	0.045
3636.14	18.729	0.018	18.252	0.014	18.212	0.019	9010.92	18.684	0.032	18.225	0.028	—	—
3741.64	18.764	0.017	18.254	0.014	18.206	0.018	9114.60	18.632	0.044	18.240	0.031	18.064	0.045
3845.66	18.739	0.017	18.271	0.014	18.239	0.018	9218.28	18.635	0.035	18.171	0.025	18.198	0.040
3952.20	18.705	0.017	18.265	0.014	18.198	0.018	9321.96	18.664	0.034	18.237	0.025	18.242	0.033
4064.00	18.719	0.017	18.281	0.012	18.210	0.015	9434.28	18.683	0.031	18.200	0.025	18.145	0.033
4166.73	18.702	0.017	18.274	0.014	18.167	0.018	9537.96	18.689	0.028	18.235	0.025	18.158	0.026
4271.62	18.738	0.017	18.264	0.014	18.226	0.018	9641.64	18.632	0.027	18.239	0.020	18.212	0.028
4377.63	18.724	0.017	18.262	0.012	18.224	0.019	9753.96	18.713	0.027	18.169	0.020	18.159	0.022
4492.97	18.708	0.015	18.274	0.015	18.167	0.019	9866.28	18.639	0.022	18.223	0.020	18.178	0.027
4596.39	18.737	0.018	18.292	0.015	18.175	0.019	9969.96	18.646	0.024	18.205	0.020	18.198	0.026
4701.80	18.718	0.018	18.243	0.015	18.217	0.019	10073.64	18.694	0.029	18.228	0.020	18.165	0.028
4807.56	18.741	0.018	18.285	0.012	18.200	0.020	10177.32	18.679	0.030	18.212	0.020	18.173	0.029
4922.04	18.736	0.018	18.248	0.015	18.226	0.017	10298.28	18.688	0.022	18.241	0.013	18.144	0.020
5024.68	18.724	0.019	18.271	0.015	18.230	0.021	10401.96	18.717	0.025	18.247	0.017	18.188	0.022
5129.57	18.692	0.018	18.275	0.015	18.190	0.020	10505.64	18.666	0.021	18.242	0.013	18.195	0.022
5235.67	18.682	0.018	18.278	0.015	18.213	0.021	10609.32	18.644	0.021	18.220	0.013	18.188	0.021